Continuum Mech. Thermodyn. (2008) 19: 399–422
DOI 10.1007/s00161-007-0061-x

ORIGINAL ARTICLE

D. D. Tjahjanto · S. Turteltaub · A. S. J. Suiker

Crystallographically based model for transformation-induced plasticity in multiphase carbon steels

Received: 5 February 2007 / Accepted: 25 October 2007 / Published online: 14 December 2007

Abstract The microstructure of multiphase steels assisted by transformation-induced plasticity consists of grains of retained austenite embedded in a ferrite-based matrix. Upon mechanical loading, retained austenite may transform into martensite, as a result of which plastic deformations are induced in the surrounding phases, i.e., the ferrite-based matrix and the untransformed austenite. In the present work, a crystallographically based model is developed to describe the elastoplastic transformation process in the austenitic region. The model is formulated within a large-deformation framework where the transformation kinematics is connected to the crystallographic theory of martensitic transformations. The effective elastic stiffness accounts for anisotropy arising from crystallographic orientations as well as for dilation effects due to the transformation. The transformation model is coupled to a single-crystal plasticity model for a face-centered cubic lattice to quantify the plastic deformations in the untransformed austenite. The driving forces for transformation and plasticity are derived from thermodynamical principles and include lower-length-scale contributions from surface and defect energies associated to, respectively, habit planes and dislocations. In order to demonstrate the essential features of the model, simulations are carried out for austenitic single crystals subjected to basic loading modes. To describe the elastoplastic response of the ferritic matrix in a multiphase steel, a crystal plasticity model for a body-centered cubic lattice is adopted. This model includes the effect of nonglide stresses in order to reproduce the asymmetry of slips in the twinning and antitwinning directions that characterizes the behavior of this type of lattices. The models for austenite and ferrite are combined to simulate the microstructural behavior of a multiphase steel. The results of the simulations show the relevance of including plastic deformations in the austenite in order to predict a more realistic evolution of the transformation process.

Keywords TRIP-assisted steel · Martensitic phase · Transformation · Crystal plasticity

PACS 61.50.Ks, 62.20.Dc, 62.20.Fe, 64.70.Kb

Communicated by S. Conti

This work is part of the research program of the Netherlands Institute for Metals Research (NIMR) and the *Stichting voor Fundamenteel Onderzoek der Materie* (FOM, financially supported by the *Nederlandse Organisatie voor Wetenschappelijk Onderzoek* (NWO)). The research was carried out under project number 02EMM20 of the FOM/NIMR program "Evolution of the Microstructure of Materials" (P-33).

D. D. Tjahjanto (✉) · S. Turteltaub · A. S. J. Suiker
Faculty of Aerospace Engineering, Delft University of Technology, Kluyverweg 1, 2629 HS Delft, The Netherlands
E-mail: d.d.tjahjanto@tudelft.nl
E-mail: s.r.turteltaub@tudelft.nl
E-mail: a.s.j.suiker@tudelft.nl

1 Introduction

Low-alloyed, multiphase carbon steels assisted by the mechanism of transformation-induced plasticity (known as *TRIP steels*) show a good combination of strength and ductility characteristics in comparison to conventional carbon steels. This class of advanced high-strength steels has a microstructure composed of ferrite, bainite (which is a composition of ferrite and cementite), and crucially for the TRIP mechanism, a dispersion of grains of retained austenite that have been preserved when the material is brought to room temperature during thermal processing (see, e.g., [18,19,27]). Although the austenitic phase is metastable at room temperature, it may transform into martensite when subjected to subsequent mechanical and/or thermal loading. The irreversible, displacive phase transformation of austenite into martensite is characterized by a crystallographic rearrangement that produces a shear deformation with respect to the habit plane (austenite–martensite interface) as well as an expansion normal to the habit plane. To accommodate this transformation, plastic deformations may develop in surrounding parts of the austenitic grain that have not (yet) transformed, as well as in the neighboring ferritic (or bainitic) grains. The rate of transformation of austenite to martensite and the amount of plasticity generated in the untransformed austenitic regions and/or the ferritic matrix depend on the resistances to plastic slip and transformation. For higher local carbon concentrations in the austenite (e.g., > 1.4 wt.%), the pinning of dislocations by interstitial carbon atoms will occur more frequently, which causes a substantial increase in the yield strength of the austenite. Under these circumstances most of the plastic deformation induced by the martensitic transformation will occur in the relatively soft ferritic phase [12]. However, a high carbon concentration may also increase the resistance to transformation, hence plastic deformations may occur in the austenitic phase despite a high yield strength [17].

In the past decades, various constitutive models have been proposed to elucidate the complex interactive mechanisms that occur in steels assisted by transformation-induced plasticity; see e.g., [4,10,11,16,21,22,26]. In most cases, the models are developed within a small-strain, isotropic elastoplasticity framework. However, this assumption may lead to inaccurate predictions, particularly for simulations at smaller length-scales (e.g., at the single-crystal level), where the effect of anisotropy due to crystallographic orientations cannot be neglected. Moreover, martensitic transformations locally can induce large elastoplastic deformations (including a rigid-body rotation) in the neighboring phases, even if the macroscopic deformation is relatively small. The purpose of the present contribution is twofold: (1) the development of crystallographically based anisotropic thermomechanical continuum models for the different phases in multiphase steels, and (2) the study of the influence of plastic deformations in the austenitic phase on the overall TRIP mechanism. The models are intended to describe the response of each phase under externally applied mechanical loading at the level of individual single-crystal grains and, consequently, provide a detailed insight into the influence of the microstructure on the overall response. For simplicity, only models for the austenitic–martensitic and ferritic phases are developed, while the other phases in the microstructure (i.e., bainite and thermal martensite) are not modeled explicitly; rather, they are implicitly lumped into the response of a ferrite-based matrix since ferrite is the dominant phase. The models for austenite–martensite and for ferrite are subsequently used in finite-element calculations of an aggregate of grains to simulate the microstructural response in a multiphase carbon steel. The model for austenite–martensite includes elastic, plastic, and transformation mechanisms and is an extension of the multiscale martensitic transformation model of Turteltaub and Suiker [28,30,31]. In that phase transformation model, the effective transformation kinematics and the effective elastic stiffness are derived from lower-scale information that follows from the crystallographic theory of martensitic transformations [1,3,14,33]. In the present contribution, this transformation model is coupled to a single-crystal plasticity model that describes the plastic slip in the face-centered cubic (FCC) austenitic phase. The coupling is done within a large-deformation framework and the criteria for transformation and plastic deformation are based on a thermodynamically consistent approach. For the ferritic phase, a single-crystal plasticity model is developed to simulate the elastoplastic behavior of body-centered cubic (BCC) crystalline structures. The BCC crystal plasticity model includes the so-called nonglide stress that accounts for the spatial spreading of the core of screw dislocations in BCC crystals [2,32].

The article is organized as follows: the elastoplastic transformation model for austenitic single crystals is derived in Sect. 2. Simulations with elementary loading conditions are presented in Sect. 3 in order to illustrate some important features of the model for austenite single crystals. In Sect. 4, simulations of multiphase TRIP steel microstructures are discussed. Some closing remarks are provided in Sect. 5. The mathematical notation used in the present article is similar to that adopted in previous works; see [28,30,31] for more details.

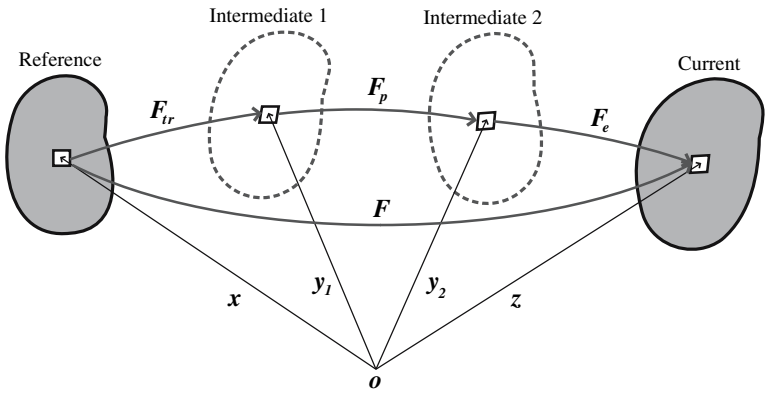

Fig. 1 Decomposition of the deformation gradient $\boldsymbol{F}$ using a reference configuration, a first and a second intermediate configuration, and a current configuration

2 Elastoplastic transformation model for the austenitic phase

In this section, a constitutive model that describes the elastoplastic transformation behavior of single-crystal austenite is developed from thermomechanical considerations. For the derivation of the constitutive model, the multiscale phase-transformation model developed previously by Turteltaub and Suiker [28,30,31] is adopted, which describes the transformation of austenite to martensite ignoring the effect of plasticity in the austenite. This model is thus intended for modeling the constitutive behavior of multiphase carbon steels and for shape-memory alloys where the generation of plasticity in the austenite does not play a significant role. The crystallographic input for the multiscale model follows from the theory of martensitic transformations [1,33]. For the transformation of FCC austenite to BCT martensite, the theory of martensitic transformations provides the habit plane vectors as well as the orientations of the martensitic twin variants for each of the 24 possible transformation systems. This information is used in an averaging scheme to simulate the effective elastic stiffness and the transformation evolution at the grain level. For simplicity reasons, compatibility requirements between the individual twin variants (see, e.g. [13,20]) are, however, not accounted for in this averaging scheme. In the thermomechanical framework presented in this section, the transformation model presented in [28,30,31] is integrated with a crystal plasticity model for FCC metals to account for the development of plastic deformations in the austenitic parent phase.

2.1 Kinematics

The kinematic description of the elastoplastic transformation deformation inside a single-crystal grain of austenite is formulated within the finite-deformation theory, where the total deformation gradient $\boldsymbol{F}$ is multiplicatively decomposed as

$$\boldsymbol{F} = \boldsymbol{F}_{\mathrm{e}}\,\boldsymbol{F}_{\mathrm{p}}\,\boldsymbol{F}_{\mathrm{tr}}\,, \tag{1}$$

where $\boldsymbol{F}_{\mathrm{e}}$, $\boldsymbol{F}_{\mathrm{p}}$, and $\boldsymbol{F}_{\mathrm{tr}}$ are the effective elastic, plastic, and transformation contributions to the total deformation gradient, respectively. This decomposition of the deformation relates to the four configurations depicted in Fig. 1, i.e., the undeformed reference configuration, two (stress-free) intermediate configurations, and the current configuration. The reference configuration is chosen to coincide with a stress-free, fully austenitic state. A detailed multiscale analysis is outside of the scope of the present work; it is assumed that lower-length-scale elastic, plastic, and transformation deformations are captured in an average sense by the corresponding deformation tensor in the decomposition (1). It is noted that the order of the decomposition in general does not correspond to the actual deformation sequence in subdomains of a material point (which is determined by the actual loading path).

For the kinematic description of transformation, lower-length-scale contributions are included through crystallographic information derived from the theory of martensitic transformations [1,33], averaged in a representative volume element centered at a material point. The effective transformation deformation gradient

is given by the sum of the transformation deformation gradients over all active martensitic transformation systems at a given material point, in accordance with [31]

$$\boldsymbol{F}_{\mathrm{tr}} = \boldsymbol{I} + \sum_{\alpha=1}^{M} \xi^{(\alpha)} \boldsymbol{b}^{(\alpha)} \otimes \boldsymbol{d}^{(\alpha)} \,, \tag{2}$$

where $\boldsymbol{I}$ is the identity tensor, $\xi^{(\alpha)} = \hat{\xi}^{(\alpha)}(\boldsymbol{x}, t)$ represents the volume fraction of a transformation system α (measured in a volume element in the reference configuration centered at $\boldsymbol{x}$ at time t), M (=24) is the total number of transformation systems, $\boldsymbol{b}^{(\alpha)}$ is the shape strain vector at the habit plane of transformation system α, and $\boldsymbol{d}^{(\alpha)}$ is the vector normal to the habit plane. The vectors $\boldsymbol{b}^{(\alpha)}$ and $\boldsymbol{d}^{(\alpha)}$, which can be obtained from the theory of martensitic transformations [1,33], are assumed to remain constant in the reference configuration throughout the deformation (hence, the present model does not include phenomena such as detwinning).

The martensitic volume fractions (at each material point and for all times) must satisfy the following constraints:

$$0 \leq \sum_{\alpha=1}^{M} \xi^{(\alpha)} \leq 1, \quad 0 \leq \xi^{(\alpha)} \leq 1, \quad 1 - \sum_{\alpha=1}^{M} \xi^{(\alpha)} = \xi_{\mathrm{A}}, \tag{3}$$

where ξ_{A} denotes the volume fraction of the austenite. Since the vectors $\boldsymbol{b}^{(\alpha)}$ and $\boldsymbol{d}^{(\alpha)}$ are assumed to be time independent, the material time derivative of the transformation deformation gradient follows from (2) as

$$\dot{\boldsymbol{F}}_{\mathrm{tr}} = \sum_{\alpha=1}^{M} \dot{\xi}^{(\alpha)} \boldsymbol{b}^{(\alpha)} \otimes \boldsymbol{d}^{(\alpha)} \,. \tag{4}$$

In carbon steels, the martensitic phase is relatively brittle with low dislocation activity, presumably due to the high levels of interstitial carbon that prevent plastic slip. Consequently, it is assumed that plastic deformations only evolve in the austenitic phase and not in the martensitic phase. Hence, the plastic deformation gradient $\boldsymbol{F}_{\mathrm{p}}$ reflects the accumulated plastic deformation in the austenite, as well as the plastic deformation that the martensitic product phase inherits from the austenitic parent phase. The evolution of the plastic deformation is described by the effective plastic velocity gradient $\boldsymbol{L}_{\mathrm{p}}$, which is measured in the second intermediate configuration and is related to the plastic deformation gradient as

$$\boldsymbol{L}_{\mathrm{p}} = \dot{\boldsymbol{F}}_{\mathrm{p}} \, \boldsymbol{F}_{\mathrm{p}}^{-1} \,. \tag{5}$$

To reflect the considerations described above, the effective plastic velocity gradient $\boldsymbol{L}_{\mathrm{p}}$ in a volume element is expressed as a weighted value of the effective plastic velocity gradient of the austenitic phase $\boldsymbol{L}_{\mathrm{pA}}$ (measured in the second intermediate configuration) as

$$\boldsymbol{L}_{\mathrm{p}} = \tilde{\xi}_{\mathrm{A}} \boldsymbol{L}_{\mathrm{pA}}, \tag{6}$$

where the weighting factor is taken as the volume fraction of austenite $\tilde{\xi}_{\mathrm{A}}$ in the second intermediate configuration. A formal relation between the volume fraction of the austenite measured in the second and reference configurations can be obtained assuming that the austenitic subdomains are connected through the effective deformation gradient $\boldsymbol{F}_{\mathrm{p}} \boldsymbol{F}_{\mathrm{tr}}$, i.e.,

$$\tilde{\xi}_{\mathrm{A}} = \left(\frac{1}{J_{\mathrm{p}} J_{\mathrm{tr}}} \right) \xi_{\mathrm{A}} = \frac{\xi_{\mathrm{A}}}{J_{\mathrm{tr}}} \,. \tag{7}$$

with $J_{\mathrm{p}} = \det \boldsymbol{F}_{\mathrm{p}}$ and $J_{\mathrm{tr}} = \det \boldsymbol{F}_{\mathrm{tr}}$ and where the second relation was derived based on an isochoric plastic deformation, i.e., $J_{\mathrm{p}} = 1$.

In accordance with crystal plasticity theory, the plastic velocity gradient of the austenite can be expressed in terms of the sum of slip rates in all possible slip systems i,

$$\boldsymbol{L}_{\mathrm{pA}} = \sum_{i=1}^{N} \dot{\gamma}_{\mathrm{A}}^{(i)} \boldsymbol{m}_{\mathrm{A}}^{(i)} \otimes \boldsymbol{n}_{\mathrm{A}}^{(i)} \,, \tag{8}$$

where $\boldsymbol{m}_{\mathrm{A}}^{(i)}$ and $\boldsymbol{n}_{\mathrm{A}}^{(i)}$ are, respectively, the unit vectors parallel to the slip direction and normal to the slip plane for slip system i (measured in the second intermediate configuration and assumed to be unchanged from the reference configuration), $\dot{\gamma}_{\mathrm{A}}^{(i)}$ reflects the slip rate of slip system i, and N (=24) is the total number of slip systems in the FCC austenite. Combining (6), (7) and (8), the effective plastic velocity gradient in the second intermediate configuration can be expressed as

$$\boldsymbol{L}_{\mathrm{p}} = \sum_{i=1}^{N} \dot{\gamma}^{(i)} \boldsymbol{m}_{\mathrm{A}}^{(i)} \otimes \boldsymbol{n}_{\mathrm{A}}^{(i)} , \tag{9}$$

where $\dot{\gamma}^{(i)}$ may be interpreted as the "effective" plastic slip rate of the austenitic slip system i, given by

$$\dot{\gamma}^{(i)} = \frac{\xi_{\mathrm{A}}}{J_{\mathrm{tr}}} \dot{\gamma}_{\mathrm{A}}^{(i)} . \tag{10}$$

2.2 Entropy

In thermomechanical processes, the entropy and temperature may be viewed as the thermal analogues of deformation and stress, respectively [6,31]. Hence, in analogy to the triple decomposition (1) of the total deformation gradient, the total entropy density per unit mass, η, is decomposed as

$$\eta = \eta_{\mathrm{e}} + \eta_{\mathrm{p}} + \eta_{\mathrm{tr}} , \tag{11}$$

where η_{e} represents the conservative (reversible) part of the entropy density, and η_{p} and η_{tr} are the entropy densities related to plasticity and phase transformation processes, respectively. The expression for the transformation entropy density η_{tr} is taken to be (see [31])

$$\eta_{\mathrm{tr}} = \sum_{\alpha=1}^{M} \xi^{(\alpha)} \frac{\lambda_T^{(\alpha)}}{\theta_T} , \tag{12}$$

where $\lambda_T^{(\alpha)}$ defines the transformation latent heat at the transformation temperature θ_T, which is the heat (per unit mass) required to transform austenite to a martensitic transformation system α at $\theta = \theta_T$. The transformation temperature θ_T is introduced as a (theoretical) temperature at which austenite can homogeneously transform into a specific martensitic transformation system α, at zero stress, without dissipation, and in the absence of an internal energy barrier. Observe in (12) that the value of θ_T is assumed to be the same for all transformation systems α. From (12), the rate of change of the transformation entropy density η_{tr} can be simply obtained as

$$\dot{\eta}_{\mathrm{tr}} = \sum_{\alpha=1}^{M} \dot{\xi}^{(\alpha)} \frac{\lambda_T^{(\alpha)}}{\theta_T} . \tag{13}$$

In addition, the effective plastic entropy density rate, $\dot{\eta}_{\mathrm{p}}$, may be connected to the plastic entropy density rate in the austenite, $\dot{\eta}_{\mathrm{pA}}$ via

$$\dot{\eta}_{\mathrm{p}} = \xi_{\mathrm{A}} \, \dot{\eta}_{\mathrm{pA}} . \tag{14}$$

This formulation is in correspondence with the absence of growth of plastic deformations in the martensite, which implies that the plastic entropy rate in that phase is zero. Hence, (14) essentially reflects a weighted average of the entropy rates, and is analogous to expression (6) for the effective plastic velocity gradient. Similar to the entropy decomposition in the isotropic plasticity model of Simo and Miehe [25], the plastic entropy rate in the austenite $\dot{\eta}_{\mathrm{pA}}$ is assumed to be dependent of the plastic deformation rate in that phase. Accordingly, the following relation is proposed:

$$\dot{\eta}_{\mathrm{pA}} = \sum_{i=1}^{N} \dot{\gamma}_{\mathrm{A}}^{(i)} \phi_{\mathrm{A}}^{(i)} , \tag{15}$$

where $\phi_{\mathrm{A}}^{(i)}$ measures the entropy related to plastic slip in system i. Note that the expression above is of a similar form to the kinematic relation (8). Substituting (15) into (14) gives

$$\dot{\eta}_{\mathrm{p}} = \xi_{\mathrm{A}} \sum_{i=1}^{N} \dot{\gamma}_{\mathrm{A}}^{(i)} \phi_{\mathrm{A}}^{(i)} \;=\; J_{\mathrm{tr}} \sum_{i=1}^{N} \dot{\gamma}^{(i)} \phi_{\mathrm{A}}^{(i)} \,, \tag{16}$$

where the right part of the expression has been computed with the use of (10).

2.3 Thermodynamical relations

To obtain the thermodynamical relations for a material point experiencing phase transformation and plasticity effects, the procedure developed by Coleman and Noll [8] is used. In this procedure, the derivation and identification of the driving forces and the corresponding fluxes for transformation and plasticity are performed within a framework that is similar to that of the simpler case of transformation without plasticity; see [31]. Let $\mathscr{D}$ be the dissipation per unit volume in the reference configuration, given by

$$\mathscr{D} := -\rho_0 \dot{\epsilon} + \rho_0 \theta \dot{\eta} + \boldsymbol{P} \cdot \dot{\boldsymbol{F}} - \nabla\theta \cdot \boldsymbol{\Phi} \,, \tag{17}$$

where ρ_0 is the mass density, $\dot{\epsilon}$ is the rate of the internal energy density, $\boldsymbol{P}$ is the first Piola–Kirchhoff stress, $\dot{\boldsymbol{F}}$ is the rate of the deformation gradient, θ is the temperature, and $\boldsymbol{\Phi}$ is the entropy flux, which are all related to the reference configuration. Using the kinematic relations (1), (4), (5), and (9), and applying the chain rule to construct the time derivative of the total deformation gradient $\boldsymbol{F}$, the internal mechanical power in (17) can be expressed as

$$\boldsymbol{P} \cdot \dot{\boldsymbol{F}} = \boldsymbol{P}\, \boldsymbol{F}_{\mathrm{tr}}^{T}\, \boldsymbol{F}_{\mathrm{p}}^{T} \cdot \dot{\boldsymbol{F}}_{\mathrm{e}} + \sum_{i=1}^{N} \tau_{\mathrm{p}}^{(i)} \dot{\gamma}^{(i)} + \sum_{\alpha=1}^{M} \tau_{\mathrm{tr}}^{(\alpha)} \dot{\xi}^{(\alpha)} \,, \tag{18}$$

where $\tau_{\mathrm{p}}^{(i)}$ and $\tau_{\mathrm{tr}}^{(\alpha)}$ are referred to as the resolved stresses on plastic slip system i and transformation system α, respectively. The resolved stress for plastic slip (i.e., the Schmid stress) has the form

$$\tau_{\mathrm{p}}^{(i)} := \boldsymbol{F}_{\mathrm{e}}^{T}\, \boldsymbol{P}\, \boldsymbol{F}_{\mathrm{tr}}^{T}\, \boldsymbol{F}_{\mathrm{p}}^{T} \cdot \left(\boldsymbol{m}_{\mathrm{A}}^{(i)} \otimes \boldsymbol{n}_{\mathrm{A}}^{(i)} \right) \,, \tag{19}$$

while the resolved stress for transformation reads

$$\tau_{\mathrm{tr}}^{(\alpha)} := \boldsymbol{F}_{\mathrm{p}}^{T}\, \boldsymbol{F}_{\mathrm{e}}^{T}\, \boldsymbol{P} \cdot \left(\boldsymbol{b}^{(\alpha)} \otimes \boldsymbol{d}^{(\alpha)} \right) \,. \tag{20}$$

Invoking (11), (13), and (16), the internal thermal power $\rho_0 \theta \dot{\eta}$ appearing in (17) can be elaborated as

$$\rho_0 \theta \dot{\eta} = \rho_0 \theta \dot{\eta}_{\mathrm{e}} + \sum_{i=1}^{N} \zeta_{\mathrm{p}}^{(i)} \dot{\gamma}^{(i)} + \sum_{\alpha=1}^{M} \zeta_{\mathrm{tr}}^{(\alpha)} \dot{\xi}^{(\alpha)} \,, \tag{21}$$

where $\zeta_{\mathrm{p}}^{(i)}$ and $\zeta_{\mathrm{tr}}^{(\alpha)}$ are the thermal analogues of the resolved stresses $\tau_{\mathrm{p}}^{(i)}$ and $\tau_{\mathrm{tr}}^{(\alpha)}$, respectively, given by

$$\zeta_{\mathrm{p}}^{(i)} := \rho_0 \theta J_{\mathrm{tr}} \phi_{\mathrm{A}}^{(i)} \quad , \quad \zeta_{\mathrm{tr}}^{(\alpha)} := \rho_0 \theta \frac{\lambda_T^{(\alpha)}}{\theta_T} \,. \tag{22}$$

As a next step, the internal energy density rate $\dot{\epsilon}$ in (17) needs to be determined, which requires a specification of the relevant state variables connected to constitutive models. The internal energy in the present model is decomposed into various mechanical and thermal contributions. As shown in subsequent sections, the bulk strain and thermal energies can be characterized by the elastic deformation gradient $\boldsymbol{F}_e$, the conservative entropy η_e, and the volume fractions of martensite $\xi^{(\alpha)}$, where henceforth the latter parameters are collected in the vector $\boldsymbol{\xi} := \{\xi^{(\alpha)}, \alpha = 1, \ldots, M\}$. Furthermore, a strain energy related to interfaces will be specified in terms of $\boldsymbol{\xi}$ and a lower-length-scale strain energy associated to dislocations will be expressed in terms of a scalar microstrain β. Correspondingly, the internal energy density ε is given by a function $\bar{\varepsilon}$ of the state variables

$\boldsymbol{F}_\mathrm{e}$, η_e, β, and $\boldsymbol{\xi}$. In addition, in accordance with the procedure of Coleman and Noll [8], it is momentarily assumed that $\bar{\varepsilon}$ also depends on the fluxes $\dot{\beta}$, $\dot{\boldsymbol{\xi}}$, and $\boldsymbol{\Phi}$, i.e.,

$$\varepsilon = \bar{\varepsilon}(\boldsymbol{F}_\mathrm{e}, \eta_\mathrm{e}, \beta, \boldsymbol{\xi}; \dot{\beta}, \dot{\boldsymbol{\xi}}, \boldsymbol{\Phi}) \,. \tag{23}$$

Observe that the volume fraction of austenite ξ_A is not used as an independent state variable since it is related to $\boldsymbol{\xi}$ via $(3)_3$. Combining (18), (21), and (23) with (17) leads to the following expression for the dissipation:

$$\begin{aligned}\mathscr{D} = &\left(\boldsymbol{P}\,\boldsymbol{F}_\mathrm{tr}^T\,\boldsymbol{F}_\mathrm{p}^T - \rho_0 \frac{\partial \bar{\varepsilon}}{\partial \boldsymbol{F}_\mathrm{e}}\right) \cdot \dot{\boldsymbol{F}}_\mathrm{e} + \rho_0 \left(\theta - \frac{\partial \bar{\varepsilon}}{\partial \eta_\mathrm{e}}\right) \dot{\eta}_\mathrm{e} + \sum_{i=1}^{N} \left(\tau_\mathrm{p}^{(i)} + \zeta_\mathrm{p}^{(i)}\right) \dot{\gamma}^{(i)} - \rho_0 \frac{\partial \bar{\varepsilon}}{\partial \beta}\,\dot{\beta} - \rho_0 \frac{\partial \bar{\varepsilon}}{\partial \dot{\beta}}\,\ddot{\beta} \\ &+ \sum_{\alpha=1}^{M} \left(\tau_\mathrm{tr}^{(\alpha)} + \zeta_\mathrm{tr}^{(\alpha)} - \rho_0 \frac{\partial \bar{\varepsilon}}{\partial \xi^{(\alpha)}}\right) \dot{\xi}^{(\alpha)} - \sum_{\alpha=1}^{M} \rho_0 \frac{\partial \bar{\varepsilon}}{\partial \dot{\xi}^{(\alpha)}}\,\ddot{\xi}^{(\alpha)} - \nabla\theta \cdot \boldsymbol{\Phi} - \rho_0 \frac{\partial \bar{\varepsilon}}{\partial \boldsymbol{\Phi}} \cdot \dot{\boldsymbol{\Phi}} \,. \end{aligned} \tag{24}$$

The second law of thermodynamics requires that the local entropy rate should be non-negative, $\Gamma \geq 0$, in any thermomechanical process, which is in correspondence with a non-negative energy dissipation, $\mathscr{D} = \Gamma\theta \geq 0$ since the temperature θ is positive. Furthermore, the terms in (24) that are multiplied by the rates $\dot{\boldsymbol{F}}_\mathrm{e}$, $\dot{\eta}_\mathrm{e}$, $\ddot{\beta}$, $\ddot{\boldsymbol{\xi}}$, and $\dot{\boldsymbol{\Phi}}$ must vanish since otherwise a process can be specified for which the dissipation is negative. These requirements result in

$$\boldsymbol{P} = \rho_0 \frac{\partial \bar{\varepsilon}}{\partial \boldsymbol{F}_\mathrm{e}} \boldsymbol{F}_\mathrm{p}^{-T}\,\boldsymbol{F}_\mathrm{tr}^{-T}, \quad \theta = \frac{\partial \bar{\varepsilon}}{\partial \eta_\mathrm{e}} \,, \tag{25}$$

and that the internal energy density ε does not depend on the fluxes $\dot{\beta}$, $\dot{\boldsymbol{\xi}}$, and $\boldsymbol{\Phi}$, i.e, $\varepsilon = \bar{\varepsilon}(\boldsymbol{F}_\mathrm{e}, \eta_\mathrm{e}, \beta, \boldsymbol{\xi})$.

In anticipation of a constitutive model for hardening (given in Sect. 2.5) and to simplify the presentation, the rate of change of the microstrain, $\dot{\beta}$, is taken to depend linearly on the rate of change of the effective plastic slips, $\dot{\gamma}^{(i)}$, i.e.,

$$\dot{\beta} = \sum_{i=1}^{N} w^{(i)} \dot{\gamma}^{(i)} \,, \tag{26}$$

where, as will be shown in Sect. 2.5, the functions $w^{(i)}$ depend nonlinearly on the slip resistance. In view of (25) and (26), the remaining nonzero terms in the dissipation expression (24) can be formally written as $\mathscr{D} = \mathscr{D}_\mathrm{tr} + \mathscr{D}_\mathrm{p} + \mathscr{D}_q$, where $\mathscr{D}_\mathrm{tr}$, $\mathscr{D}_\mathrm{p}$, and $\mathscr{D}_q$ are the dissipations due to phase transformation, plastic deformation, and heat conduction, respectively, as given by

$$\mathscr{D}_\mathrm{tr} := \sum_{\alpha=1}^{M} f^{(\alpha)} \dot{\xi}^{(\alpha)}, \quad \mathscr{D}_\mathrm{p} := \sum_{i=1}^{N} g^{(i)} \dot{\gamma}^{(i)}, \quad \mathscr{D}_q := -\nabla\theta \cdot \boldsymbol{\Phi} \,. \tag{27}$$

Here, $f^{(\alpha)}$ and $g^{(i)}$ are the driving forces for transformation and plasticity, respectively, in accordance with

$$f^{(\alpha)} := \tau_\mathrm{tr}^{(\alpha)} + \zeta_\mathrm{tr}^{(\alpha)} - \rho_0 \frac{\partial \bar{\varepsilon}}{\partial \xi^{(\alpha)}}, \quad g^{(i)} := \tau_\mathrm{p}^{(i)} + \zeta_\mathrm{p}^{(i)} - \rho_0 \frac{\partial \bar{\varepsilon}}{\partial \beta} w^{(i)} \,. \tag{28}$$

In the present study, it is assumed that the dissipation inequality $\mathscr{D} = \mathscr{D}_\mathrm{tr} + \mathscr{D}_\mathrm{p} + \mathscr{D}_q \geq 0$ holds for the plasticity, transformation, and heat conduction processes independently, i.e.,

$$\mathscr{D}_\mathrm{tr} \geq 0 \,, \quad \mathscr{D}_\mathrm{p} \geq 0, \quad \mathscr{D}_q \geq 0 \,. \tag{29}$$

For further elaborations it is convenient to use the Helmholtz energy density ψ instead of the internal energy ε. Assuming a one-to-one relation between the temperature and the conservative entropy, the Helmholtz energy density can be derived from the internal energy density using the following Legendre transformation:

$$\bar{\psi}(\boldsymbol{F}_\mathrm{e}, \theta, \beta, \boldsymbol{\xi}) = \bar{\varepsilon}(\boldsymbol{F}_\mathrm{e}, \tilde{\eta}_\mathrm{e}(\boldsymbol{F}_\mathrm{e}, \theta, \beta, \boldsymbol{\xi}), \beta, \boldsymbol{\xi}) - \theta \tilde{\eta}_\mathrm{e}(\boldsymbol{F}_\mathrm{e}, \theta, \beta, \boldsymbol{\xi}) \,, \tag{30}$$

in which, for generality, η_e is assumed to be a function of all state variables, $\eta_\mathrm{e} = \tilde{\eta}_\mathrm{e}(\boldsymbol{F}_\mathrm{e}, \theta, \beta, \boldsymbol{\xi})$. From the requirement of material frame indifference, the elastic deformation gradient $\boldsymbol{F}_\mathrm{e}$ cannot be arbitrarily used

as a state variable in the Helmholtz (or the internal) energy density; instead, an elastic strain measure based purely on the stretch part of deformation must be used. For this purpose, the elastic Green–Lagrange strain $\boldsymbol{E}_{\mathrm{e}} = \frac{1}{2}(\boldsymbol{F}_{\mathrm{e}}^T \boldsymbol{F}_{\mathrm{e}} - \boldsymbol{I})$ is introduced. With this deformation measure, an alternative form $\hat{\psi}$ of the Helmholtz energy density function is considered, such that

$$\hat{\psi}(\boldsymbol{E}_{\mathrm{e}}, \theta, \beta, \boldsymbol{\xi}) = \bar{\psi}(\boldsymbol{F}_{\mathrm{e}}, \theta, \beta, \boldsymbol{\xi}) \,. \tag{31}$$

The work-conjugated stress measure associated to $\boldsymbol{E}_{\mathrm{e}}$ is the second Piola–Kirchhoff stress $\boldsymbol{S}$ in the second intermediate configuration, which is related (by definition) to the first Piola–Kirchhoff stress $\boldsymbol{P}$ as

$$\boldsymbol{S} := \frac{1}{J_{\mathrm{tr}}} \boldsymbol{F}_{\mathrm{e}}^{-1} \boldsymbol{P} \boldsymbol{F}_{\mathrm{tr}}^T \boldsymbol{F}_{\mathrm{p}}^T \,. \tag{32}$$

Taking derivatives with respect to $\boldsymbol{F}_{\mathrm{e}}$ and η_{e} in (30) and (31), together with applying the chain rule in the expression for $\boldsymbol{E}_{\mathrm{e}}$, and further using (25) and (32), it can be shown that the pairs $\boldsymbol{S}$ and $\boldsymbol{E}_{\mathrm{e}}$, and η_{e} and θ are related as follows:

$$\boldsymbol{S} = \rho_2 \frac{\partial \hat{\psi}}{\partial \boldsymbol{E}_{\mathrm{e}}} \,, \quad \eta_{\mathrm{e}} = -\frac{\partial \hat{\psi}}{\partial \theta} \,, \tag{33}$$

where $\rho_2 = \rho_0 / J_{\mathrm{tr}}$ (with $J_{\mathrm{tr}} = \det \boldsymbol{F}_{\mathrm{tr}}$) denotes the mass density in the second intermediate configuration. Furthermore, taking the partial derivatives of $\hat{\psi}$ with respect to $\boldsymbol{\xi}$ and β and using $(25)_2$ and $(33)_2$, it can also be shown that the expressions (28) for the driving forces for transformation $f^{(\alpha)}$ and plasticity $g^{(i)}$ can alternatively be written as

$$f^{(\alpha)} = \tau_{\mathrm{tr}}^{(\alpha)} + \zeta_{\mathrm{tr}}^{(\alpha)} - \rho_0 \frac{\partial \hat{\psi}}{\partial \xi^{(\alpha)}}, \quad g^{(i)} = \tau_{\mathrm{p}}^{(i)} + \zeta_{\mathrm{p}}^{(i)} - \rho_0 \frac{\partial \hat{\psi}}{\partial \beta} w^{(i)} \,. \tag{34}$$

2.4 Specification of the Helmholtz energy density

A specific form of the Helmholtz energy $\hat{\psi}(\boldsymbol{E}_{\mathrm{e}}, \theta, \beta, \boldsymbol{\xi})$ can be constructed as an extension of the form proposed in [30,31] by incorporating the contribution of the defect energy related to dislocations. Consequently, the Helmholtz energy is assumed to have the following form:

$$\hat{\psi}(\boldsymbol{E}_{\mathrm{e}}, \theta, \beta, \boldsymbol{\xi}) = \hat{\psi}_m(\boldsymbol{E}_{\mathrm{e}}, \boldsymbol{\xi}) + \hat{\psi}_{\mathrm{th}}(\theta, \boldsymbol{\xi}) + \hat{\psi}_{\mathrm{s}}(\boldsymbol{\xi}) + \hat{\psi}_{\mathrm{d}}(\beta, \boldsymbol{\xi}) \,, \tag{35}$$

where $\hat{\psi}_m$ is the bulk elastic strain energy, $\hat{\psi}_{\mathrm{th}}$ is the thermal energy, $\hat{\psi}_s$ is a surface energy term, and $\hat{\psi}_{\mathrm{d}}$ is the defect energy related to dislocations. The specific forms of the bulk strain energy and thermal energy in (35) are as follows:

$$\hat{\psi}_m(\boldsymbol{E}_{\mathrm{e}}, \boldsymbol{\xi}) = \frac{1}{2\rho_2} \mathbb{C}(\boldsymbol{\xi}) \boldsymbol{E}_{\mathrm{e}} \cdot \boldsymbol{E}_{\mathrm{e}} \;=\; \frac{1}{2\rho_0} J_{\mathrm{tr}}(\boldsymbol{\xi}) \mathbb{C}(\boldsymbol{\xi}) \boldsymbol{E}_{\mathrm{e}} \cdot \boldsymbol{E}_{\mathrm{e}} \,, \tag{36}$$

$$\hat{\psi}_{\mathrm{th}}(\theta, \boldsymbol{\xi}) = h(\boldsymbol{\xi}) \left((\theta - \theta_T) - \theta \ln \frac{\theta}{\theta_T} \right) - \eta_T \theta + \sum_{\alpha=1}^{M} \xi^{(\alpha)} \lambda_T^{(\alpha)} \,, \tag{37}$$

where $\mathbb{C} = \mathbb{C}(\boldsymbol{\xi})$ is the effective fourth-order elasticity tensor and $h = h(\boldsymbol{\xi})$ is the effective specific heat capacity per unit mass. The elasticity tensor $\mathbb{C}(\boldsymbol{\xi})$ and the specific heat $h(\boldsymbol{\xi})$ reflect that the properties of a material point evolve with the martensitic volume fractions $\boldsymbol{\xi}$. The parameter η_T is the conservative entropy measured at the transformation temperature θ_T. The energy densities $\hat{\psi}_m$ and $\hat{\psi}_{\mathrm{th}}$ are constructed, respectively, from the following mechanical constitutive relation between the second Piola–Kirchhoff stress in the second intermediate configuration and the elastic Green–Lagrange strain, and the thermal constitutive relation between the conservative entropy η_{e} and the temperature θ:

$$\boldsymbol{S} = \mathbb{C} \boldsymbol{E}_{\mathrm{e}}, \quad \eta_{\mathrm{e}} = h \ln \left(\frac{\theta}{\theta_T} \right) + \eta_T \,. \tag{38}$$

The specific forms of the effective elastic stiffness tensor and the effective specific heat are adopted from Turteltaub and Suiker [31], i.e.,

$$\mathbb{C} = \frac{1}{J_{\mathrm{tr}}}\left(\xi_{\mathrm{A}}\mathbb{C}^{A} + (1+\delta_T)\sum_{\alpha=1}^{M}\xi^{(\alpha)}\mathbb{C}^{(\alpha)}\right), \quad h = \xi_{\mathrm{A}}h_{\mathrm{A}} + \sum_{\alpha=1}^{M}\xi^{(\alpha)}h^{(\alpha)}\,. \tag{39}$$

In the above equation, $\mathbb{C}^A$ is the stiffness tensor of the FCC austenite, which is determined by three independent elastic coefficients κ_j^A, with $j \in \{1, 2, 3\}$. The stiffness tensor $\mathbb{C}^{(\alpha)}$ refers to twinned martensite (transformation system α), which depends on six independent elastic coefficients, κ_j^M, with $j \in \{1, 2, \ldots 6\}$ as well as on the proportions and orientations of two twin-related BCT martensitic variants, which can be obtained from the theory of martensitic transformations [1,33]. In addition, the parameter δ_T in (39) measures the volumetric growth associated to each transformation system α, in accordance with $\delta_T = \boldsymbol{b}^{(\alpha)} \cdot \boldsymbol{d}^{(\alpha)}$, which is identical for all martensitic system $\alpha = 1, \ldots, M$. Further, the coefficient h_{A} reflects the specific heat of the austenite and $h^{(\alpha)}$ is the specific heat of the martensitic transformation system α.

The surface energy density $\hat{\psi}_{\mathrm{s}}$ is related to the local deformation field required to maintain a coherent interface between the austenitic parent phase and the martensitic product phase, and is described by means of the phenomenological model proposed by Turteltaub and Suiker [30,31], i.e.,

$$\hat{\psi}_{\mathrm{s}}(\boldsymbol{\xi}) = \frac{\chi}{\rho_0 l_0}\sum_{\alpha=1}^{M}\xi^{(\alpha)}\left(1-\xi^{(\alpha)}\right), \tag{40}$$

where χ is an interface energy per unit area and l_0 is a length-scale parameter representing the volume-to-surface ratio of a circular platelet of martensite within a spherical grain of austenite.

In addition to the bulk elastic strain energy density, a lower-scale elastic strain energy density is introduced that accounts for the elastic distortion of the lattice due to the presence of dislocations, i.e., the defect energy. Since in the present model the kinetics of dislocations is not resolved explicitly, a simple isotropic phenomenological model commonly used in the materials science literature is adopted to account for the elastic energy generated by dislocations [15]. In accordance with this model, the elastic energy associated to a single dislocation is given by $\frac{1}{2}\omega\mu b^2$, where μ is an equivalent (isotropic) shear modulus, b is the magnitude of the Burger's vector, and ω is a dimensionless scaling factor. An expression for the defect energy in a volume element can be obtained as $\frac{1}{2}\omega_{\mathrm{A}}\mu b^2\rho_{\mathrm{d}}$, where ρ_{d} is a measure of the total dislocation line length per unit volume in the second intermediate configuration and ω_{A} is a scaling factor for the strain energy of an assembly of dislocations. For notational convenience, it is useful to introduce a strain-like internal variable $\beta := b\sqrt{\rho_{\mathrm{d}}}$. Hence, in analogy to the bulk strain energy density (36), which depends quadratically on the elastic deformation measure $\boldsymbol{E}_{\mathrm{e}}$, the microstrain energy density depends quadratically on β, i.e.,

$$\hat{\psi}_{\mathrm{d}}(\beta, \boldsymbol{\xi}) = \frac{1}{2\rho_2}\,\omega_{\mathrm{A}}\,\mu(\boldsymbol{\xi})\,\beta^2 \;= \frac{1}{2\rho_0}\,J_{\mathrm{tr}}(\boldsymbol{\xi})\,\omega_{\mathrm{A}}\,\mu(\boldsymbol{\xi})\,\beta^2\,. \tag{41}$$

Similar to the effective elasticity tensor given by (39), the effective equivalent shear modulus $\mu = \mu(\boldsymbol{\xi})$ is expressed as

$$\mu = \frac{1}{J_{\mathrm{tr}}}\left(\xi_{\mathrm{A}}\mu_{\mathrm{A}} + (1+\delta_T)\sum_{\alpha=1}^{M}\xi^{(\alpha)}\mu^{(\alpha)}\right), \tag{42}$$

where μ_{A} and $\mu^{(\alpha)}$ are the equivalent isotropic shear moduli of the austenite and the martensitic transformation system α, respectively. The moduli μ_{A} and $\mu^{(\alpha)}$ are determined from the anisotropic elasticity tensors $\mathbb{C}^A$ and $\mathbb{C}^{(\alpha)}$ following the procedure outlined in [30]. Accordingly, in the present study, the shear moduli $\mu^{(\alpha)}$ are taken the same for all transformation systems, i.e., $\mu^{(\alpha)} = \mu_M$ for all $\alpha = 1, \ldots, M$.

It is noted that the thermal energy (37) contains terms that do not contribute to the conservative part of the entropy but that are chosen such that the transformation driving force $f^{(\alpha)}$ is consistent with the definition of the transformation temperature θ_T. Under the condition of a dissipation-free process, the driving force should be zero, $f^{(\alpha)} = 0$, since $\dot{\xi}^{(\alpha)} > 0$ during transformation. For a transformation process taking place at zero driving force there is indeed no internal energy barrier that resists the transformation. If, in addition, the surface energy and defect energy contributions to the transformation vanish (i.e., $\chi \to 0$ in (40) and $\beta = 0$ in (41)),

the transformation occurs in a homogeneous fashion. When it is further required that the stress remains zero, this means that its evolution is completely driven by the thermal energy (37). Hence, in the theoretical limit of a homogeneous, dissipation-free transformation process at zero stress, the driving force at the transformation temperature θ_T must satisfy the condition

$$f^{(\alpha)}\Big|_{\boldsymbol{E}_\mathrm{e}=\boldsymbol{0},\theta=\theta_T,\beta=0,\chi\to 0} = 0\,, \tag{43}$$

for all $\alpha = 1,\ldots,M$. Note that the zero-stress condition is reflected in (43) by $\boldsymbol{E}_\mathrm{e} = \boldsymbol{0}$. Although it is not demonstrated in detail, the above condition is indeed satisfied using the expression for the driving force presented in next section.

2.5 Driving forces, nucleation criteria, kinetic laws, and evolution of microstrain

In this section, the driving forces, nucleation criteria, and kinetic laws for the martensitic transformation process and the plastic deformation process are formulated. The driving forces for transformation and plasticity are given by $(34)_{1,2}$, and can be further elaborated by substituting the specific form for the Helmholtz energy, (35), which together with (19), (20), (22), and (32) leads to

$$f^{(\alpha)} = f_\mathrm{m}^{(\alpha)} + f_\mathrm{th}^{(\alpha)} + f_\mathrm{s}^{(\alpha)} + f_\mathrm{d}^{(\alpha)}, \quad g^{(i)} = g_\mathrm{m}^{(i)} + g_\mathrm{th}^{(i)} + g_\mathrm{d}^{(i)}, \tag{44}$$

where the mechanical bulk contribution, the thermal contribution, the surface energy contribution, and the defect energy contribution to the transformation driving force $f^{(\alpha)}$ are given, respectively, by

$$\begin{aligned}
f_\mathrm{m}^{(\alpha)} &:= J_\mathrm{tr}\boldsymbol{F}_\mathrm{p}^T\boldsymbol{F}_\mathrm{e}^T\boldsymbol{F}_\mathrm{e}\boldsymbol{S}\boldsymbol{F}_\mathrm{p}^{-T}\boldsymbol{F}_\mathrm{tr}^{-T}\cdot\left(\boldsymbol{b}^{(\alpha)}\otimes\boldsymbol{d}^{(\alpha)}\right) + \frac{1}{2}\left(\mathbb{C}_\mathrm{A} - (1+\delta_T)\mathbb{C}^{(\alpha)}\right)\boldsymbol{E}_\mathrm{e}\cdot\boldsymbol{E}_\mathrm{e}\,,\\
f_\mathrm{th}^{(\alpha)} &:= \rho_0\left(h^{(\alpha)} - h_\mathrm{A}\right)\left(\theta\ln\frac{\theta}{\theta_T} - (\theta-\theta_T)\right) + \rho_0\frac{\lambda_T^{(\alpha)}}{\theta_T}(\theta-\theta_T)\,,\\
f_\mathrm{s}^{(\alpha)} &:= -\frac{\chi}{l_0}\left(1-2\xi^{(\alpha)}\right),\\
f_\mathrm{d}^{(\alpha)} &:= \frac{\omega_\mathrm{A}}{2}\left(\mu_\mathrm{A} - (1+\delta_T)\mu^{(\alpha)}\right)\beta^2.
\end{aligned} \tag{45}$$

In addition, the mechanical bulk contribution, the thermal contribution, and the defect energy contribution to the driving force for plasticity $g^{(i)}$ read, respectively,

$$g_m^{(i)} := J_\mathrm{tr}\boldsymbol{F}_\mathrm{e}^T\boldsymbol{F}_\mathrm{e}\boldsymbol{S}\cdot\left(\boldsymbol{m}_\mathrm{A}^{(i)}\otimes\boldsymbol{n}_\mathrm{A}^{(i)}\right), \quad g_\mathrm{th}^{(i)} := \rho_0\theta J_\mathrm{tr}\phi_\mathrm{A}^{(i)}, \quad g_d^{(i)} := -J_\mathrm{tr}\,\omega_\mathrm{A}\mu\,\beta w^{(i)}\,. \tag{46}$$

If the transformation driving force $f^{(\alpha)}$ exceeds a critical value $f_\mathrm{cr}^{(\alpha)}$, the transformation process in system α is activated and the growth rate of the volume fraction, $\dot{\xi}^{(\alpha)}$, is related to the driving force for transformation $f^{(\alpha)}$ through the following kinetic relation (see also [28–31]):

$$\dot{\xi}^{(\alpha)} = \begin{cases} \dot{\xi}_0\tanh\left(\dfrac{f^{(\alpha)} - f_\mathrm{cr}^{(\alpha)}}{\nu f_\mathrm{cr}^{(\alpha)}}\right) & \text{if} \quad f^{(\alpha)} \geq f_\mathrm{cr}^{(\alpha)}\,,\\ 0 & \text{otherwise,}\end{cases} \tag{47}$$

where $\dot{\xi}_0$ is the maximum value of the transformation rate and ν is a dimensionless, viscosity-like parameter. Essentially, the critical value $f_\mathrm{cr}^{(\alpha)}$ comprises all energy contributions to the transformation kinetics that are not specified in the driving force $f^{(\alpha)}$.

The plasticity driving force $g^{(i)}$ relates to a microscale representative volume that contains both austenite and martensite. Nonetheless, since it is assumed that the martensite does not experience plastic deformations, it is natural to describe the evolution of plastic slip by means of a driving force (and an energetically conjugated internal variable) that relates to the subvolume occupied only by austenite. For this purpose, expression $(27)_2$

for the plastic dissipation is revisited, and reformulated in terms of a plastic driving force $g_{\mathrm{A}}^{(i)}$ and a plastic slip rate $\dot{\gamma}_{\mathrm{A}}^{(i)}$ that correspond to the austenitic microscale volume, i.e.,

$$\mathscr{D}_{\mathrm{p}} = \sum_{i=1}^{N} g^{(i)} \dot{\gamma}^{(i)} = \xi_{\mathrm{A}} \sum_{i=1}^{N} g_{\mathrm{A}}^{(i)} \dot{\gamma}_{\mathrm{A}}^{(i)} \,. \tag{48}$$

Essentially, the right part of this expression includes the plastic dissipation $\sum_{i=1}^{N} g_{\mathrm{A}}^{(i)} \dot{\gamma}_{\mathrm{A}}^{(i)}$, measured per unit austenite volume in the reference configuration, which is multiplied by the austenite volume fraction ξ_{A} in the reference configuration to construct the "effective" plastic dissipation $\mathscr{D}_{\mathrm{p}}$, measured per unit total volume in the reference configuration. Inserting the kinematic expression (10) into (48) leads to the following expression for the plasticity driving force $g_{\mathrm{A}}^{(i)}$ of slip system i:

$$g_{\mathrm{A}}^{(i)} = J_{\mathrm{tr}}^{-1} \, g^{(i)} \,, \tag{49}$$

where $g^{(i)}$ is given by $(44)_2$. The occurrence of plastic slip is evaluated by comparing the plasticity driving force $g_{\mathrm{A}}^{(i)}$ in (49) to the resistance against plastic slip, $s_{\mathrm{A}}^{(i)}$. The evolution of the slip resistance $\dot{s}_{\mathrm{A}}^{(i)}$ is computed with the hardening model of Peirce et al. [24] as

$$\dot{s}_{\mathrm{A}}^{(i)} = \sum_{j=1}^{N} H_{\mathrm{A}}^{(i,j)} \dot{\gamma}_{\mathrm{A}}^{(j)} \,, \tag{50}$$

where $H_{\mathrm{A}}^{(i,j)}$ is a matrix containing the hardening moduli of the austenite (with the diagonal terms referring to self-hardening and the off-diagonal terms referring to cross-hardening), i.e.,

$$\begin{array}{ll} H_{\mathrm{A}}^{(i,j)} = q_{\mathrm{A}} k_{\mathrm{A}}^{(j)} & \text{for} \quad i \neq j \,, \\ H_{\mathrm{A}}^{(i,j)} = k_{\mathrm{A}}^{(j)} & \text{for} \quad i = j \,. \end{array} \tag{51}$$

Here, q_{A} is the latent hardening ratio, which reflects the ratio between cross- and self-hardening, and $k_{\mathrm{A}}^{(j)}$ is the single-slip hardening modulus of slip system j. The initial values for $s_{\mathrm{A}}^{(i)}$ are given by $s_{\mathrm{A}}^{(i)}(t=0) = s_{\mathrm{A},0}$ (i.e., they are taken identical for all slip systems). The evolution of the single-slip hardening modulus is supposed to follow a power law, as proposed by Brown et al. [5]:

$$k_{\mathrm{A}}^{(j)} = k_0^A \left(1 - \frac{s_{rmA}^{(j)}}{s_{\infty}^{A}} \right)^{u_{\mathrm{A}}} \,, \tag{52}$$

where k_0^A is a reference hardening modulus, s_{∞}^{A} is the hardening saturation value, and u_{A} is the hardening exponent.

Plastic slip occurs when the driving force exceeds the critical resistance against slip, i.e., $g_{\mathrm{A}}^{(i)} \geq s_{\mathrm{A}}^{(i)}$. The evolution of plastic slip is simulated through a rate-dependent formulation [9,23], i.e.,

$$\dot{\gamma}_{\mathrm{A}}^{(i)} = \begin{cases} \dot{\gamma}_0^A \left(\left(\dfrac{g_{\mathrm{A}}^{(i)}}{s_{\mathrm{A}}^{(i)}} \right)^{(1/n_{\mathrm{A}})} - 1 \right) & \text{if} \quad g_{\mathrm{A}}^{(i)} \geq s_{\mathrm{A}}^{(i)} \,, \\ 0 & \text{otherwise,} \end{cases} \tag{53}$$

where $\dot{\gamma}_0^A$ and n_{A} are the reference slip rate and the rate-sensitivity exponent, respectively. Note that the kinetic relation (53) always leads to $\dot{\gamma}_{\mathrm{A}}^{(i)} \geq 0$, so that positive and negative senses of slip need to be accounted for separately. As $\dot{\gamma}_0^A \to \infty$ and/or $n_{\mathrm{A}} \to 0$, the kinetic relation (53) reduces to a rate-independent model.

To complete the formulation of the model, a constitutive relation for the evolution of the microstrain variable β and the specification of the functions $w^{(i)}$ in (26) are required. Since it is assumed that new dislocations are only generated in the austenitic region, the effective microscopic strain rate $\dot{\beta}$ in a volume element can be expressed, in analogy to (6), as

$$\dot{\beta} \;=\; \tilde{\xi}_{\mathrm{A}} \dot{\beta}_{\mathrm{A}} \;=\; \frac{\xi_{\mathrm{A}}}{J_{\mathrm{tr}}} \dot{\beta}_{\mathrm{A}} \,, \tag{54}$$

where the weighting factor $\tilde{\xi}_{\mathrm{A}}$ is the volume fraction of austenite in the second intermediate configuration and $\dot{\beta}_{\mathrm{A}}$ is the time derivative of β in the austenitic region. Note that the second relation in (54) has been constructed using (7). In line with the model proposed by Clayton [7], the state variable β_{A} is constitutively related to the average slip resistance $s_{\mathrm{A}}^{(i)}$ via the rate equation

$$c_{\mathrm{A}}\mu_{\mathrm{A}}\dot{\beta}_{\mathrm{A}} = \frac{1}{N}\sum_{i=1}^{N}\dot{s}_{\mathrm{A}}^{(i)} \,, \tag{55}$$

where μ_{A} is the equivalent isotropic shear modulus of the austenite and c_{A} is a scaling factor that accounts for dislocation interactions. The assumption of isotropy in the constitutive relation (55) may be somewhat strong, but is made here for simplicity reasons. Combining (50), (54), and (55) with (10), the effective microscopic elastic strain rate in the austenite can be formulated as

$$\dot{\beta} = \frac{1}{c_{\mathrm{A}}\mu_{\mathrm{A}}N}\sum_{i=1}^{N}\sum_{j=1}^{N}H_{\mathrm{A}}^{(i,j)}\dot{\gamma}^{(j)} \,, \tag{56}$$

which, in view of (26), indicates that the functions $w^{(i)}$ appearing in $(46)_3$, can be expressed as

$$w^{(i)} = \frac{1}{c_{\mathrm{A}}\mu_{\mathrm{A}}N}\sum_{j=1}^{N}H_{\mathrm{A}}^{(j,i)} \,. \tag{57}$$

In summary, Eqs. (44), (45), and (46) are used to compute the driving forces for transformation and plasticity and the relations (47), (53) and (56), together with the activation criteria and the hardening relations, allow one to determine the evolution of the volume fractions of martensite, the plastic slips, and the microstrain.

3 Stress–strain response of single-crystal austenite

In order to illustrate the basic features of the elastoplastic transformation model, in this section the mechanical response of a single crystal of austenite is studied numerically for several elementary loading cases. In order to solve the nonlinear, coupled evolution equations, a robust, fully implicit algorithm was implemented in a finite-element code, in an analogous fashion to the numerical formulation presented in [28] for a phase-transformation model without the effect of plasticity in the austenite. In these analyses, three different crystallographic orientations are considered that, in terms of Euler angles that follow a so-called "323" rotation sequence about the global axes, are: (0°, 0°, 0°), (45°, 0°, 0°), and (45°, 35.26°, 0°). These three orientations are such that the global $\boldsymbol{f}_1$-axis corresponds to the $[100]_{\mathrm{A}}$, $[110]_{\mathrm{A}}$, and $[111]_{\mathrm{A}}$ directions, respectively, as shown in Fig. 2, where the Miller indices refer to the austenite lattice basis. The three loading cases considered in the simulations are: (1) uniaxial tension (and compression) along the $\boldsymbol{f}_1$-axis, (2) simple shear in the direction of the $\boldsymbol{f}_1$-axis, and (3) volumetric expansion. It is noted, however, that the simulations presented here for loading along the $[111]_{\mathrm{A}}$ axis are slightly different from those presented in [28,30,31] since the in-plane orientation of the crystal (i.e., perpendicular to the $[111]_{\mathrm{A}}$-axis) given by the Euler angles (45°, 35.26°, 0°) is different from the in-plane orientation used in the aforementioned references.

3.1 Model parameters for austenite and martensite

The simulations are carried out under isothermal conditions at an ambient temperature of $\theta = 300\,\mathrm{K}$. The density of the austenite in the reference configuration is assumed to be equal to the characteristic density of a carbon steel, ρ_0=7,800 kg/m^3. The material parameters and initial values used in the simulations are listed in Table 1. These parameters are representative of the high-carbon retained austenite present in multiphase carbon steels. The carbon concentration in the austenite is taken as 1.4 wt.%, which is in close correspondence with the values measured experimentally in various high-strength TRIP steels [17,27]. The vectors $\boldsymbol{b}^{(\alpha)}$ and $\boldsymbol{m}^{(\alpha)}$ of the 24 martensitic transformation systems, which appear in (4), follow from the theory of martensitic transformations, where the Kurdjumov–Kaminsky relations are applied to relate the specific carbon concentration of 1.4 wt.% to the austenite and martensite lattice parameters. More details on this procedure and a complete

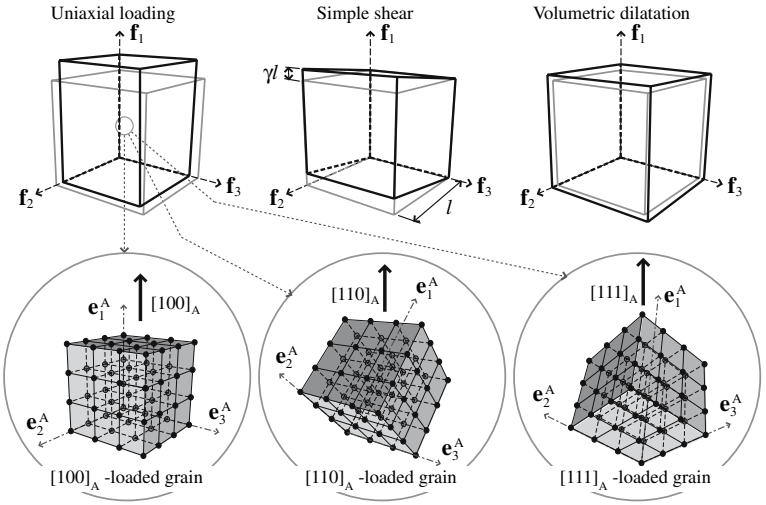

Fig. 2 Loading modes applied to the single-crystal austenite sample, and the crystallographic orientations of the sample with respect to the global $\boldsymbol{f}_1$-axis

Table 1 Material parameters for the elastoplastic transformation model

Parameter(s)	Value(s)	Equation(s)
Elastic moduli austenite	$\kappa_1^A = 286.8$, $\kappa_2^A = 166.4$, $\kappa_3^A = 145.0$ [GPa]	(39)
Elastic moduli martensite	$\kappa_1^M = 372.4$, $\kappa_2^M = 345.0$, $\kappa_3^M = 191.0$, $\kappa_4^M = 508.4$, $\kappa_5^M = 201.9$, $\kappa_6^M = 229.5$ [GPa]	(39)
Thermal driving forces ($\theta = 300$ K)	$f_{\text{th}}^{(\alpha)} = 286$, $g_{\text{A,th}}^{(i)} = \rho_0 \theta \phi_{\text{A}}^{(i)} = 12$ [MPa]	$(45)_2$, $(46)_2$, (49)
Transformation kinetic law	$\dot{\xi}_0 = 0.003\ \text{s}^{-1}$, $\nu = 0.17$, $f_{\text{cr}}^{(\alpha)} = 306$ [MPa]	(47)
Surface energy	$\chi = 0.2\ \text{J m}^{-2}$, $l_0 = 0.05\ \mu$m	(40)
Hardening law	$s_{\text{A},0} = 189$, $s_\infty^A = 579$ [MPa], $k_0^A = 3$ [GPa], $u_{\text{A}} = 2.8$, $q_{\text{A}} = 1$	(48), (52)
Plasticity kinetic law	$\dot{\gamma}_0^A = 0.001\ \text{s}^{-1}$, $n_{\text{A}} = 0.02$	(53)
Defect energy	$\beta_{\text{A},0} = 0.0056$, $c_{\text{A}} = 0.5$, $\omega_{\text{A}} = 10$ $\mu_{\text{A}} = 67.5$, $\mu^{(\alpha)} = \mu_{\text{M}} = 98.4$ [GPa]	(55)–(57)

list of the $\boldsymbol{b}^{(\alpha)}$ and $\boldsymbol{m}^{(\alpha)}$ vectors can be found in previous works [28,30,31]. Background information about the calibration of the material parameters for the elastic, transformation, and surface energies can be found in [30]. Although the procedure used to estimate the elastic stiffnesses for the austenite and the martensite shown in Table 1 is similar to that used in [30], the values presented here are somewhat different from those reported in [30]. This difference stems from a reinterpretation of the carbon content, i.e., the values in [30] were calibrated using experimental data from [12], which relate to a carbon concentration of 0.92 wt.% instead of 1.4 wt.%. Similarly, the values indicated in Table 1 of the thermal driving force $f_{\text{th}}^{(\alpha)}$ at 300 K and the critical value f_{cr} used in the transformation kinetic law were obtained using the same approach as in [30] but with a different extrapolation in terms of the carbon content. In particular, these quantities were obtained with an estimated value for the latent heat at the transformation temperature of $\lambda_T = -67$ kJ/kg and a martensite start temperature $M_s = 257$ K (see [30]). The vectors $\boldsymbol{m}_{\text{A}}^{(i)}$ and $\boldsymbol{n}_{\text{A}}^{(i)}$ of the 24 slip systems of FCC austenite, which appear in (9), relate to the family of {111} planes with slip occurring in the ⟨110⟩ directions. Since metastable retained austenite in a multiphase carbon steel cannot be produced separately from its ferritic matrix, it is difficult to obtain experimental data to characterize the plastic behavior of the austenite. Furthermore, since transformation and plastic deformation can occur simultaneously, it is not a straightforward procedure to extract the individual contributions from experimental data. An additional complication is the lack of single-crystal stress–strain data for the austenitic phase. To overcome these difficulties, the material parameters related to the plastic response of the austenite are calibrated using a stress–strain curve that is assumed to represent a purely elastoplastic

behavior (i.e., a curve where the transformation mechanism is momentarily ignored). The curve is assumed to be representative of a randomly oriented polycrystal. Such an ideal uniaxial tension curve is obtained by scaling the elastoplastic stress–strain response of a polycrystalline ferritic matrix (see also Sect. 4). The scaling factor, taken to be 2.4, is established based on the ratio between the microhardnesses of the individual ferritic and austenitic phases, which were determined from nanoindentation tests reported in the literature [12] and extrapolated for a carbon concentration of 1.4 wt.% Subsequently, the present model is applied to simulate an ideal nontransforming, randomly oriented austenitic polycrystal, employing a Taylor-type average with an artificially high transformation barrier to suppress the transformation mechanism in the simulation. Setting $q_{\mathrm{A}} = 1$ for cross-hardening, the remaining parameters for hardening and the plasticity kinetic law are determined by matching the Taylor-type curve and the scaled curve. The calibration procedure also requires the values of the defect energy parameters and the thermal contribution to the plastic driving force. In Table 1, the parameter $\beta_{\mathrm{A},0} := \beta_{\mathrm{A}}(t = 0)$ reflects the initial value of the microscopic strain measure β_{A}. Through (55), this value may be related to a common initial value $s_{A,0}$ for the slip resistance as follows: $s_{A,0} = \beta_{A,0} c_{\mathrm{A}} \mu_{\mathrm{A}}$. Furthermore, the equivalent isotropic shear moduli μ_{A} and μ_M of the austenite and martensite are calculated by matching the eigenvalues of the corresponding isotropic stiffness tensors to those of the anisotropic stiffness tensors $\mathbb{C}^A$ and $\mathbb{C}^{(\alpha)}$ in (39); see [30] for more details on this procedure. The parameter ω_{A} appearing in the defect energy (41), the term c_{A} that appears in the evolution of the microstrain (55), and the value $\phi_{\mathrm{A}}^{(i)}$ of the entropy change per unit slip, see (15), are not easy to determine. To estimate these values the following heuristic approach is used: (1) ω_{A} is chosen such that the order of magnitude of the defect energy remains a relatively small fraction of the bulk strain energy for a typical range of values of $\boldsymbol{E}_{\mathrm{e}}$ and β (see (36) and (41)) and (2) the terms c_{A} and $\phi_{\mathrm{A}}^{(i)}$ are chosen such that the contributions from the thermal and defect energies to the plastic driving force (i.e., $g_{\mathrm{th}}^{(i)}$ and $g_{\mathrm{d}}^{(i)}$ in (46)) are each about 10% of the initial value of the critical resistance against plastic slip. The idea behind the first assumption is that, although the defect energy is not negligible, it is in general not the dominant term in the Helmholtz energy. Similarly, the purpose of the second assumption is to guarantee that, for typical simulations, the dominant term for plastic deformation will be the Schmid stress. Although this procedure has some drawbacks (i.e., the uncertainty in some parameters is significant), it is taken due to the lack of direct measurements of these model parameters at the single-crystal level. Nevertheless, it is assumed that the material parameters related to plasticity (i.e., hardening law, kinetic law, and defect energy) obtained from this calibration procedure, as shown in Table 1, are representative of the plastic deformation of retained austenite.

3.2 Uniaxial tension and compression

The austenitic single-crystal configuration is represented by a cubic sample with sides of length l, which is uniaxially loaded up to an axial nominal strain $\varepsilon_{11} = \pm 0.12$ (tension or compression) using a strain rate of $10^{-4}\,\mathrm{s}^{-1}$. The nominal strain tensor is defined as $\boldsymbol{\varepsilon} := \boldsymbol{V} - \boldsymbol{I}$, where $\boldsymbol{V}$ is the left stretch tensor in the polar decomposition of the deformation gradient $\boldsymbol{F}$. The uniaxial loading condition is realized as follows. On three mutually perpendicular faces of the cubic sample the displacement normal to each of these faces is set to zero, and the normal displacement u_1 at the top surface is prescribed to be

$$u_1 = \begin{cases} 10^{-4}\, lt & \text{for tension}\,, \\ -10^{-4}\, lt & \text{for compression}\,, \end{cases} \tag{58}$$

with time t running from 0 to 1200 s. The tangential tractions on these four faces are set to zero, and the two remaining faces are traction-free. Although, due to the anisotropy of the sample, the above loading conditions do not exactly correspond to uniaxial tension (or compression), the deviation from an average uniaxial stress state is found to be small. The austenitic crystal is initially stress-free, and the analyses are performed under isothermal conditions at an ambient temperature of 300 K.

Figures 3a, b show the axial Cauchy stress T_{11} and the total martensite volume fraction ξ_{M}, given by

$$\xi_{\mathrm{M}} := \sum_{\alpha=1}^{M} \xi^{(\alpha)}\,, \tag{59}$$

which are plotted against the axial nominal strain ε_{11}. The curves plotted with thick lines and identified with a case number for each orientation relate to the responses computed with the present elastoplastic transformation

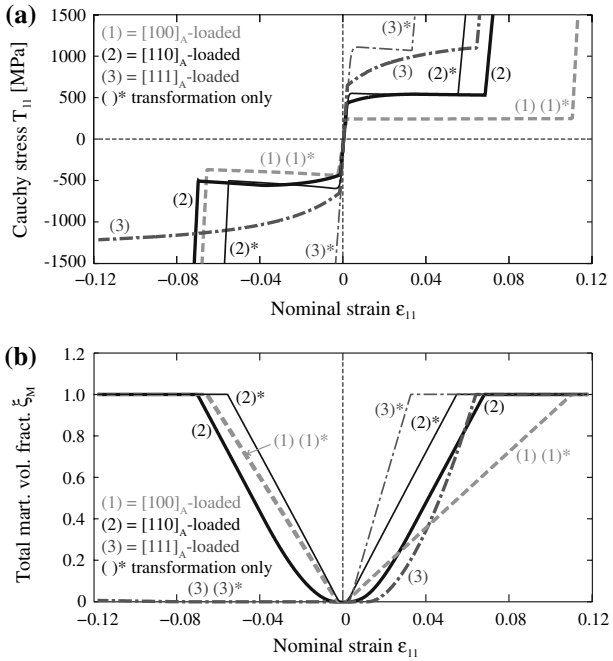

Fig. 3 Axial Cauchy stress T_{11} (**a**) and total martensite volume fraction ξ_M (**b**) versus the axial nominal strain ε_{11} for samples with different crystallographic orientations loaded under uniaxial tension and compression. The *thick* curves relate to the present elastoplastic transformation model and the *thin* curves (with an *asterisk* attached to their number) correspond to the elastic transformation model of Turteltaub and Suiker [28,30,31] that neglects the effect of plasticity in the austenite

model, and the curves plotted with thin lines and an asterisk attached to the case number reflect the responses calculated by the elastic transformation model presented in [28,30,31]. The latter curves, which are depicted for comparison, ignore the effect of plasticity in the austenite. Although not shown in Fig. 3b, the individual martensitic transformation systems active during transformation are the same for both models.

From Fig. 3a it is observed that for both models the stress–strain responses are composed of three stages, which can be identified by an abrupt change in their slopes, both in tension and compression. Initially the austenite responds elastically until the stress level in the austenite either exceeds the yield stress or the transformation threshold (i.e., when the stress is such that $f^{(\alpha)} > f_{\text{cr}}$ in the transformation model without plasticity or when either $f^{(\alpha)} > f_{\text{cr}}$ or $g_{\text{A}}^{(i)} > s_{\text{A}}^{(i)}$ in the transformation model with plasticity, for some transformation system(s) α or some slip system(s) i). Subsequently, an inelastic (plastic and/or transformation) stage follows, which finally turns back into an elastic stage when the austenite has fully transformed into martensite.

For the sample loaded in the $[100]_{\text{A}}$ direction, the responses related to the transformation models with and without plasticity coincide (i.e., curves 1 and 1* in Fig. 3a), which indicates that for this crystal orientation plasticity does not occur under uniaxial tension and compression. This feature of the $[100]_{\text{A}}$-loaded sample is due to the transformation developing at a considerably lower stress than the initial yield stress of the austenite. For the $[110]_{\text{A}}$-loaded sample, the elastic response changes into an elastoplastic response when the stress level in the austenite exceeds the initial plastic yield stress for that orientation. In this case, the plastic deformation in the austenite starts before transformation, as indicated by the initial plastic yield stress of curve 2 being lower than the initial transformation stress of curve 2* (both in tension and compression). A similar situation occurs for the $[111]_{\text{A}}$-loaded sample in tension, although in this case the initial plastic yield stress is considerably lower than the corresponding initial transformation stress (see curves 3 and 3*). For the $[111]_{\text{A}}$-loaded sample subjected to uniaxial compression, virtually no transformation occurs, which essentially means that for the grain it is energetically more favorable to deform plastically in the austenitic phase than to transform.

Both the $[110]_{\text{A}}$- and $[111]_{\text{A}}$-loaded samples show that, when the loading is increased beyond the initial yield level, the stress in the austenitic grain predicted by the elastoplastic transformation model increases due to plastic hardening. At a certain stage, the transformation driving force in one or more transformation systems exceeds the critical transformation threshold, and a martensitic transformation is initiated. Although initially the transformation process takes place at a relatively low rate, see Fig. 3b, it gradually starts to dominate the response, as indicated by the appearance of a stress plateau in the stress–strain response. Note that the stress

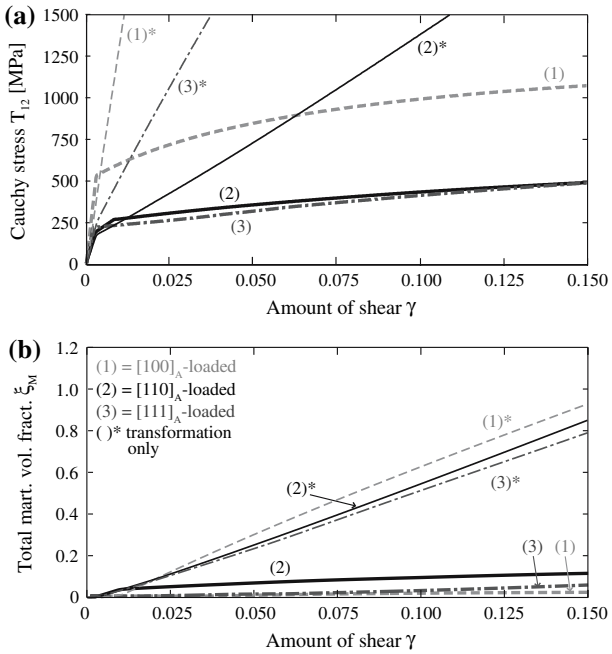

Fig. 4 Cauchy shear stress T_{12} (**a**) and total martensite volume fraction ξ_{M} (**b**) versus the amount of shear γ for samples with different crystallographic orientations loaded under simple shear. The *thick* curves relate to the present elastoplastic transformation model and the *thin* curves (with an asterisk attached to their number) correspond to the elastic transformation model of Turteltaub and Suiker [28,30,31] that neglects plasticity in the austenite

level at which the martensitic transformation is completed is virtually the same for the transformation models with and without the effect of plasticity in the austenite.

In Fig. 3b, the point where ξ_{M} becomes nonzero corresponds to the onset of transformation and the point where $\xi_{\mathrm{M}} = 1$ relates to the completion of transformation. The largest influence of the plastic deformation on the transformation behavior is observed for the $[111]_{\mathrm{A}}$-loaded crystal. In particular, from curves 3 (with plasticity) and 3* (without plasticity) in Fig. 3b, it can be observed that the plastic deformation in the austenite delays the onset of transformation in tension up to approximately 1.2% axial deformation (versus approximately 0.3% for the case without plasticity) and delays the completion of transformation up to about 6.3% strain (versus approximately 3.3% for the case without plasticity).

3.3 Simple shear

The single-crystal austenitic sample is now loaded in simple shear by applying a deformation $\boldsymbol{z} = \hat{\boldsymbol{z}}(\boldsymbol{x})$ given in components with respect to the global axes as follows (see also Fig. 2):

$$\hat{z}_1(\boldsymbol{x}) = x_1 + \gamma x_2, \quad \hat{z}_2(\boldsymbol{x}) = x_2, \quad \hat{z}_3(\boldsymbol{x}) = x_3. \tag{60}$$

The parameter γ represents the amount of shear, and the shearing rate corresponds to $\dot{\gamma} = 10^{-4}\ \mathrm{s}^{-1}$. The samples are deformed up to $\gamma = 0.15$. The results are presented in Fig. 4 by plotting the Cauchy shear stress T_{12} and the total martensitic volume fraction ξ_M versus the amount of shear γ. As for the uniaxial loading case, the thick curves relate to the present elastoplastic transformation model and the thin curves correspond to the elastic transformation model of Turteltaub and Suiker [28,30,31] that neglects plasticity in the austenite.

The stress–strain curves shown in Fig.4a for the transformation model without plasticity (curves 1*, 2*, and 3*) indicate a significantly stiff response. This is due to the fact that the transformation mechanism, which involves volumetric expansion, is not ideally suited to accommodate the imposed deformation in simple shear, which is an isochoric deformation mode. To preserve the (overall) isochoric deformation, a complex internal distribution of elastic strains is required to balance the volumetric expansion due to transformation. Although transformation is not an optimal deformation mechanism for simple shear, it is more favorable than a pure elastic deformation and, consequently, the transformation-only model predicts that transformation does occur,

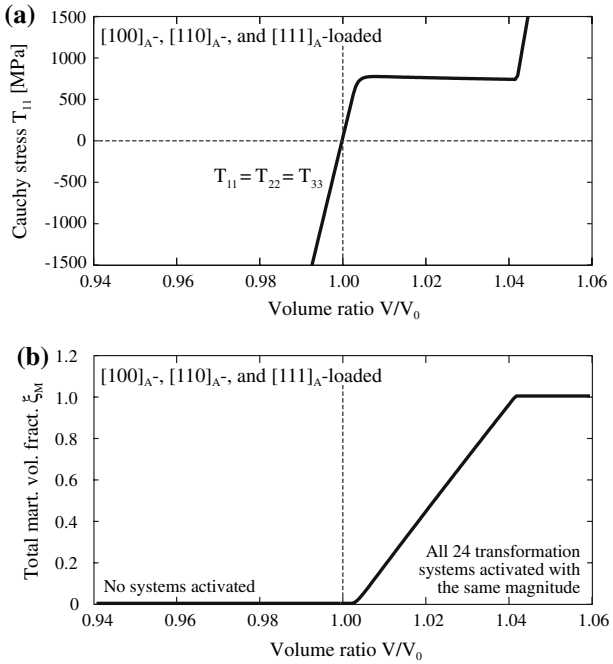

Fig. 5 Normal Cauchy stress $T_{11}(= T_{22} = T_{33})$ (**a**) and total martensite volume fraction ξ_{M} (**b**) versus volume ratio V/V_0 for samples with different crystallographic orientations loaded under volumetric expansion and volumetric contraction. Because plasticity in the austenite is not activated, the present elastoplastic transformation model provides the same result as the elastic transformation model of Turteltaub and Suiker [28,30,31]

albeit at a relatively slow rate compared to, for example, uniaxial extension (compare curves 1*, 2*, and 3* in Figs. 3b and 4b).

The transformation rates predicted by the present transformation model with plasticity (curves 1, 2, and 3 in Fig. 4b) are significantly lower than those predicted by the transformation-only model, which indicates that the inelastic deformation under simple shear is dominated by an (isochoric) plastic deformation in the austenitic phase. Hence, in addition of not being an efficient deformation mechanism under simple shear, the martensitic transformation process is here further suppressed by plastic deformations. As shown in Fig. 4b, at $\gamma = 0.15$ the largest volume fraction of martensite observed in the simulations is close to 0.1 for the sample loaded in shear along the $[110]_{\mathrm{A}}$ direction. Accordingly, for the crystal orientations and the strain range shown in Fig. 4a, the responses under simple shear obtained with the present elastoplastic transformation model are in fact close to the predictions of a classical elastoplastic model for an FCC single crystal and significantly less stiff than the corresponding curves for the transformation-only model.

3.4 Volumetric expansion and contraction

The response of the samples under volumetric expansion is simulated by imposing the deformation $\boldsymbol{z} = \hat{\boldsymbol{z}}(\boldsymbol{x})$, given in components as

$$\hat{z}_1(\boldsymbol{x}) = \lambda x_1, \quad \hat{z}_2(\boldsymbol{x}) = \lambda x_2, \quad \hat{z}_3(\boldsymbol{x}) = \lambda x_3, \tag{61}$$

where λ represents the principal stretch, with $\lambda > 1$ for expansion and $\lambda < 1$ for contraction. The volume ratio V/V_0 is equal to λ^3, where V is the current volume and V_0 is the initial volume. The applied deformation rate equals $\dot{\lambda} = 10^{-4}\ \mathrm{s}^{-1}$. The computational results are presented in Fig. 5, showing the normal component T_{11} of the Cauchy stress tensor (note that $T_{11} = T_{22} = T_{33}$) and the total martensitic volume fraction ξ_M as functions of the volume ratio V/V_0.

It can be observed that the responses under volumetric expansion and contraction are independent of the crystallographic orientation of the austenitic sample. During volumetric expansion the austenitic sample initially responds elastically, but transforms into martensite when the transformation threshold is reached. The phase transformation occurs at constant stress, as indicated by the stress plateau in Fig. 5, where all

transformation systems $\alpha = 1, \ldots, M$ are activated equally and no plastic slip is observed. The absence of plastic slip can be ascribed to the fact that the deviatoric part of the loading is zero. When the transformation is complete, the stress again raises in accordance with the elastic characteristics of the martensitic product phase. In addition, under volumetric contraction neither transformation nor plasticity occurs; the sample remains in the austenitic phase and contracts elastically. The absence of transformation is due to the fact that a martensitic transformation is accompanied by volumetric growth, a mechanism that clearly cannot occur during volumetric contraction.

4 Stress–strain response of TRIP steel microstructures

In multiphase TRIP steel microstructures, islands of retained austenite are frequently surrounded by ferritic grains. In the present study, the anisotropic elastoplastic response of the ferritic grains will be described by a crystal plasticity model similar to the one used for the FCC austenite. The present formulation is an extension of the model for BCC ferrite presented in [29], in the sense that the driving force here includes, in addition to the resolved stress, thermal and defect energy contributions.

Most of the formulation of the elastoplastic model for the BCC ferrite can be derived in a similar fashion as for the elastoplastic transformation model for austenite given in Sect. 2, by suppressing the transformation contribution. This can be formally achieved by eliminating the volume fractions as state variables, and setting $\boldsymbol{F}_{\mathrm{tr}} = \boldsymbol{I}$ and $\eta_{\mathrm{tr}} = 0$. Accordingly, the Helmholtz energy of the ferrite, $\psi_{\mathrm{F}} = \hat{\psi}_{\mathrm{F}}(\boldsymbol{E}_{\mathrm{e}}, \theta, \beta_{\mathrm{F}})$, can be derived from that of austenite given by (35), using $J_{\mathrm{tr}} = 1$, omitting the surface energy and the latent heat, and replacing ρ_0, $\mathbb{C}$, h, ω_{A}, μ, β, θ_T, and η_T by ρ_0^{F}, $\mathbb{C}^{\mathrm{F}}$, h_{F}, ω_{F}, μ_{F}, β_{F}, θ_{F}, and η_{F}, respectively, with the superscript/subscript "F" indicating the ferrite. The mechanical and thermal constitutive relations of the ferrite are analogous to (38), where the stiffness tensor $\mathbb{C}^F$ of the cubic ferrite is characterized by three independent stiffness coefficients, κ_j^F, with $j \in \{1, 2, 3\}$. The evolutions of the slip resistance and the plastic slip occur in analogy with Eqs. (50)–(53).

In addition, the evolution of the microstrain parameter $\dot{\beta}_{\mathrm{F}}$ as a function of $\dot{\gamma}_{\mathrm{F}}^{(i)}$ is defined in a similar fashion as (56). The asymmetry of slips in the twinning and antitwinning directions, which is typical for a BCC lattice, can be accounted for through the kinetic law (53), by substituting, instead of the classical resistance $s_{\mathrm{F}}^{(i)}$, an "effective" slip resistance $\tilde{s}_{\mathrm{F}}^{(i)}$ (see Vitek et al. [2,32]):

$$\tilde{s}_{\mathrm{F}}^{(i)} = s_F^{(i)} - \tilde{a}^{(i)} \tilde{\tau}_{\mathrm{F}}^{(i)} \,. \tag{62}$$

Here, $\tilde{a}^{(i)}$ is a coefficient that gives the net effect of the nonglide stress on the effective resistance, and $\tilde{\tau}_{\mathrm{F}}^{(i)}$ is the nonglide stress of slip system i, given by

$$\tilde{\tau}_{\mathrm{F}}^{(i)} = \boldsymbol{F}_{\mathrm{e}}^T \, \boldsymbol{F}_{\mathrm{e}} \, \boldsymbol{S} \cdot (\boldsymbol{m}_{\mathrm{F}}^{(i)} \otimes \tilde{\boldsymbol{n}}_{\mathrm{F}}^{(i)}) \,. \tag{63}$$

Note that the expression for the nonglide stress is formally similar to expression $(46)_1$ of the resolved stress, with the normal to the nonglide plane $\tilde{\boldsymbol{n}}_{\mathrm{F}}^{(i)}$ in (63) playing an equivalent role as the normal $\boldsymbol{n}_{\mathrm{F}}^{(i)}$ to the actual slip plane.

The mechanical behavior of a TRIP steel is studied considering a microstructural cubic sample composed of an austenitic grain surrounded by six ferritic grains and subjected to uniaxial tension, see Fig. 6. The loading is applied until a total nominal axial strain of 0.15 is reached. The boundary conditions and loading rate on each face of the cube are similar to those of the single-crystalline austenitic sample, as described in Sect. 3.2. Furthermore, the analyses are performed under isothermal conditions, at an ambient temperature of $\theta = 300\,\mathrm{K}$. At the onset of loading, the austenite grain is stress-free and occupies approximately 13% of the total domain Ω. The sides of the cubic sample have a length of $L = 3\,\mu\mathrm{m}$ and the base of the polyhedral austenitic grain has a square base with a side length of $2\,\mu\mathrm{m}$ (see Fig. 6). This characteristic grain size is in close correspondence with average grain sizes reported in experimental works on TRIP steels [12,27].

The response of the austenitic region is described by the elastoplastic transformation model presented in Sect. 2, and the material parameters for this model are the same as for the single-crystal computations, see Table 1. The response of the ferritic grains is simulated by the BCC crystal plasticity model outlined above, and the model parameters are listed in Table 2. The mass density of the ferrite (in the reference configuration) is taken equal to the one for austenite, i.e., ρ_0^{F}=7800 kg/m^3. A complete list of the vectors $\boldsymbol{m}_{\mathrm{F}}^{(i)}$ and $\boldsymbol{n}_{\mathrm{F}}^{(i)}$ as

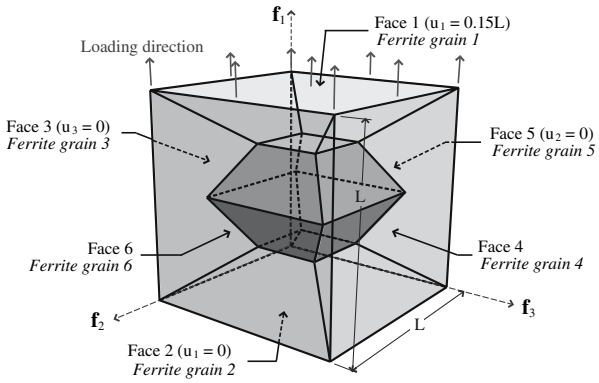

Fig. 6 Geometry and boundary conditions for a TRIP steel microstructural sample consisting of a single grain of retained austenite (positioned at the center, plotted in *grey*) embedded in a matrix of six ferritic grains

Table 2 Material parameters for the BCC crystal plasticity model

Parameter(s)	Value(s)	Equation(s) with A → F
Elastic moduli ferrite	$\kappa_1^{\mathrm{F}} = 233.5$, $\kappa_2^{\mathrm{F}} = 135.5$, $\kappa_3^{\mathrm{F}} = 118.0$ [GPa]	(38)
Thermal driving force ($\theta = 300$ K)	$\zeta_{\mathrm{F}}^{(i)} = \rho_0^{\mathrm{F}}\, \theta\, \phi_{\mathrm{F}}^{(i)} = 10$ MPa	$(46)_2$
Hardening law	$s_{\mathrm{F},0} = 154$, $s_{\infty}^{\mathrm{F}} = 412$ [MPa]	(50)–(52)
	$k_0^{\mathrm{F}} = 1.9$ GPa, $u_{\mathrm{F}} = 2.8$, $q_{\mathrm{F}} = 1$	
Plasticity kinetic law	$\dot{\gamma}_0^{\mathrm{F}} = 0.001\ \mathrm{s}^{-1}$, $n_{\mathrm{F}} = 0.02$	(53)
Nonglide stress coefficient	$\tilde{a}^{(i)} = 0.12$	(62)
Defect energy	$\omega_{\mathrm{F}} = 7$, $\beta_{\mathrm{F},0} = 0.0056$, $c_{\mathrm{F}} = 0.5$	$(45)_4$, (55)–(57)
	$\mu_{\mathrm{F}} = 55.0$ GPa	

well as a discussion on the choice of the contributing slip systems for the BCC ferrite lattice can be found in [29]. The elastic properties and the calibration of the model parameters for the plastic behavior are similar to those reported in [29]. Nevertheless, some of the values shown in Table 2 for the hardening law and the plastic kinetic law are different from those given in [29] since the calibration procedure used here is based on a plastic driving force that includes, in addition to the Schmid stress, contributions from the thermal and defect energies (which were not taken into account in [29]). In that sense, the model parameters related to the thermal driving force and the defect energy are required for the calibration. The parameter $\beta_{\mathrm{F},0}$ given in Table 2 represents the initial value of the microscopic strain measure β_{F}. From (55), with $A \rightarrow F$, this value may be related to a common initial value $s_{\mathrm{F},0}$ for the slip resistance as follows: $s_{\mathrm{F},0} = \beta_{\mathrm{F},0}\, c_{\mathrm{F}}\, \mu_{\mathrm{F}}$. The equivalent isotropic shear modulus μ_{F} of the ferrite is calculated through matching the eigenvalues of the corresponding isotropic stiffness tensor to those of the anisotropic stiffness tensor $\mathbb{C}^{\mathrm{F}}$; see [30] for more details. Finally, the values for c_{F}, ω_{F} and $\phi_{\mathrm{F}}^{(i)}$ were estimated using the same assumptions as those presented in Sect. 3.1 for the austenitic phase.

4.1 A single grain of austenite embedded in a matrix of uniformly oriented ferritic grains

The analyses presented in this section refer to the case where the sample in Fig. 6 consists of a single grain of austenite surrounded by six uniformly oriented grains of ferrite. Two crystallographic orientations for the ferritic grains are considered in the simulations such that the global loading direction $\boldsymbol{f}_1$ corresponds, respectively, to the $[100]_{\mathrm{F}}$ and $[111]_{\mathrm{F}}$ directions. The subscript "F" indicates that the Miller indices refer to the ferritic lattice basis. Each uniform orientation of the ferritic grains is combined with three orientations of the austenitic grain, which are chosen such that the global loading direction $\boldsymbol{f}_1$ corresponds, respectively, to the $[100]_{\mathrm{A}}$, $[110]_{\mathrm{A}}$ and $[111]_{\mathrm{A}}$ directions, where the subscript "A" indicates the local austenitic lattice basis. This leads to a total of six combinations of grain orientations, which will be referred to as cases 1a–c and 2a–c, respectively. Cases 1a, b, and c refer, respectively, to the three orientations of the austenitic grain mentioned

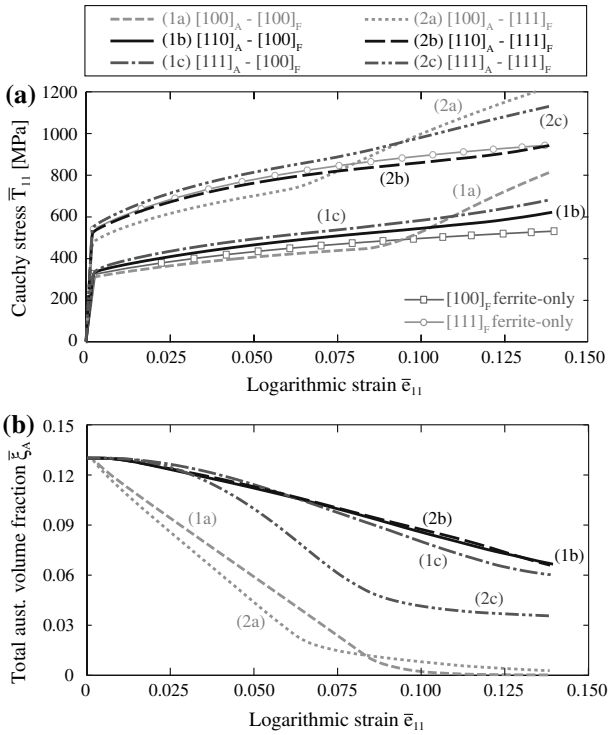

Fig. 7 Effective axial stress–strain response (**a**) and total austenite volume fraction (**b**) of a sample containing a single grain of retained austenite embedded in a matrix of six uniformly oriented ferritic grains, see Fig. 6

above, each combined with uniformly oriented grains of ferrite for which the global vector $\boldsymbol{f}_1$ corresponds to $[100]_\mathrm{F}$, whereas cases 2a, b, and c refer, respectively, to the three orientations of the austenitic grain combined with uniformly oriented grains of ferrite where $\boldsymbol{f}_1$ corresponds to $[111]_\mathrm{F}$.

The responses for the six cases are depicted in Fig. 7, which shows the effective axial Cauchy stress $\bar{T}_{11}$ and the effective austenite volume fraction $\bar{\xi}_\mathrm{A}$ plotted against the effective axial logarithmic strain $\bar{e}_{11}$. The logarithmic strain tensor is defined as $\boldsymbol{e} := \ln \boldsymbol{V}$, where $\boldsymbol{V}$ is the left stretch tensor. The effective axial Cauchy stress $\bar{T}_{11}$ and the effective axial logarithmic strain $\bar{e}_{11}$ are computed by averaging, respectively, the local axial Cauchy stress T_{11} and the local axial logarithmic strain e_{11} over the sample volume in the current configuration. Similarly, the effective austenite volume fraction $\bar{\xi}_\mathrm{A}$ is obtained by averaging the local austenite fraction ξ_A, as given by

$$\xi_\mathrm{A}(\boldsymbol{x}) := \begin{cases} 1 - \xi_M(\boldsymbol{x}) & \text{for} \quad \boldsymbol{x} \in \Omega_\mathrm{A}\,, \\ 0 & \text{for} \quad \boldsymbol{x} \in \Omega_F\,, \end{cases} \tag{64}$$

with respect to the total sample volume in the reference configuration. In (64), Ω_A and Ω_F represent the domains occupied by the austenitic grain and the ferritic matrix in the reference configuration, respectively. For comparison purposes, the elastoplastic responses of a pure ferritic sample loaded in the $[100]_\mathrm{F}$ and $[111]_\mathrm{F}$ directions are also shown in Fig. 7a.

Since the ferrite occupies most of the samples' volume (i.e., 87%), the influence of the orientation of the ferritic grains on the stress–strain response is, during the early stages of the deformation, more significant than the influence of the orientation of the austenitic grains. Indeed, as shown in Fig. 7a, the stress–strain curves for cases 1a–c (i.e., samples with a ferritic matrix loaded in the $[100]_\mathrm{F}$ direction) tend to be clustered initially around the curve for pure ferrite loaded in the $[100]_\mathrm{F}$ direction. Similarly, the curves for cases 2a–c (i.e., samples with a ferritic matrix loaded in the $[111]_\mathrm{F}$ direction) tend to be clustered initially around the corresponding curve of a purely ferritic material. Hence, the higher effective yield strength observed in cases 2a–c, in comparison to cases 1a–c, is clearly related to the fact that the ferrite loaded in the $[111]_\mathrm{F}$ direction is "strong" and the ferrite loaded in the $[100]_\mathrm{F}$ direction is "weak". The samples with the $[100]_\mathrm{A}$-loaded austenite grain and ferritic matrices loaded in the $[100]_\mathrm{F}$ and $[111]_\mathrm{F}$ directions (cases 1a and 2a, respectively) initially have a lower effective strength compared to the corresponding benchmark curves of pure ferrite. Hence, the presence of

Table 3 Orientations of the ferritic grains expressed in terms of the "323" Euler rotation angles for samples consisting of a grain of retained austenite surrounded by six ferritic grains (see Fig. 6)

Grain	Multiple orientation (MO) 1	Multiple orientation (MO) 2
1	(0.0, 0.0, 0.0)	(45.0, 0.0, 0.0)
2	(45.0, 0.0, 0.0)	(0.0, 0.0, 0.0)
3	(45.0, 35.26, 0.0)	(45.0, 17.63, 0.0)
4	(22.5, 0.0, 0.0)	(45.0, 35.26, 0.0)
5	(22.5, 17.63, 0.0)	(22.5, 0.0, 0.0)
6	(45.0, 17.63, 0.0)	(22.5, 17.63, 0.0)

retained austenite initially has a detrimental effect on the effective strength. Nonetheless, at larger deformations the responses show a rapid increase in stress and eventually provide an effective strength that is higher than that of the samples with the $[110]_A$- and $[111]_A$-loaded austenitic grains (see Fig. 7a). This is because the austenitic grain loaded in the $[100]_A$ direction has the highest transformation rate (see Fig. 7b) and, after full transformation into a relatively stiff martensitic phase, deforms elastically, thereby monotonically increasing the effective strength of the sample. More specifically, at the end of the loading process, the samples with the $[100]_A$-loaded grain contain the highest amount of martensite (about 13% since the austenite has nearly fully transformed into martensite; see Fig. 7b), and therefore have the highest effective strength. In contrast, the samples with the $[110]_A$-loaded grain at this stage contain the lowest amount of martensite (i.e., about 6% martensite and thus 7% untransformed austenite; see curves 1b and 2b in Fig. 7b), and consequently have the lowest effective strength of the six loading cases analyzed.

The strength of the samples containing a grain of austenite loaded in the $[110]_A$ direction lies either above or below the ferrite-only strength (i.e., cases 1b and 2b, respectively) depending on whether the ferritic matrix is relatively "weak" (case 1b) or relatively "strong" (case 2b). In contrast, over the whole deformation range, the samples with a $[111]_A$-loaded austenite grain (cases 1c and 2c) show a higher effective strength than the corresponding benchmark case of a ferrite-only material. In comparison to the response of single-crystalline austenite loaded under uniaxial tension, the transformation of $[110]_A$- and $[111]_A$-loaded austenitic grains embedded in a ferritic matrix occurs rather slowly (compare cases 1b and 2b in Fig. 7b to case 2 in Fig. 3b as well as cases 1c and 2c to case 3). Observe that, although the plastic deformation in the austenite delays the transformation compared to the transformation-only model, in all single-crystal simulations the transformation is eventually completed within the imposed strain range (i.e., at 12% strain the single crystal has fully transformed for all cases plotted in Fig. 3b). In contrast, the inclusion-matrix simulations of the $[110]_A$- and $[111]_A$-loaded austenitic grains are far from complete at the end of the simulation. This reduction in the amount of martensite generated can be attributed to two effects: (1) the constraint imposed by the ferritic matrix, which opposes the volumetric expansion and shear from the transforming austenitic grain, and (2) the reduction of the available transformation driving force due to plastic dissipation in the ferritic grains as well as in the untransformed austenite.

4.2 A single grain of austenite embedded in a ferritic matrix with multiple orientations

In this section, simulations of a single grain of austenite within a ferritic matrix composed of six grains with different crystallographic orientations are performed. The orientations of the ferritic grains are chosen such that they are evenly distributed in the orientation space constructed by the Euler angles. Similar to the simulations in the previous section, the austenitic grain is loaded either in the $[100]_A$, $[110]_A$, or $[111]_A$ direction. In Table 3, the crystallographic orientations of the ferrite grains are given in terms of the "323" Euler angles. In addition, to study the influence of the spatial distribution of the ferritic grains, two different ferritic matrices are considered, indicated by "MO1" and "MO2" in Table 3. The matrices MO1 and MO2 are composed of ferritic grains with similar crystallographic orientations, but with the spatial arrangement of the grains being different. The two spatial arrangements of the six ferritic grains, arbitrarily chosen among the $6! = 720$ possible combinations, are meant to be illustrative rather than comprehensive.

Figure 8a shows the effective axial Cauchy stress $\bar{T}_{11}$, and Fig. 8b shows the total austenitic volume fraction $\bar{\xi}_A$, both plotted against the effective axial logarithmic strain $\bar{e}_{11}$. As can be observed from the figures, the transformation process in the samples with the MO2 ferritic matrix (curves 4a–c) occurs somewhat faster than in the samples with the MO1 ferritic matrix (curves 3a–c), which gives the samples with the MO2 ferritic matrix a slightly larger effective strength (e.g., about 7% higher when comparing cases 3c and 4c at the end

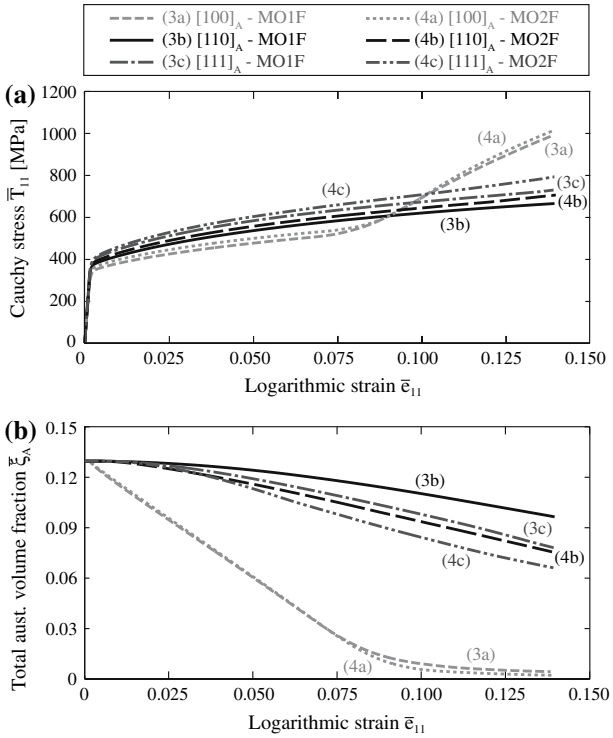

Fig. 8 Effective axial stress–strain response and total austenite volume fraction of a single grain of retained austenite embedded in a matrix of ferritic grains with multiple orientations

of the loading process). As for the matrix of uniformly oriented grains, during the first stage of deformation the highest effective strength relates to the samples with a $[111]_A$-loaded austenitic grain (cases 3c and 4c), followed by the samples with a $[110]_A$-loaded austenitic grain (cases 3b and 4b), and the samples with a $[100]_A$-loaded austenitic grain (cases 3a and 4a). At the final stage of deformation a rapid increase of the effective hardening is found for the samples with a $[100]_A$-loaded austenitic grain, which is related to the large amount of martensite present in these samples. The results further indicate that the effect of the orientation of the austenitic grain on the overall response is qualitatively the same for the MO1 and MO2 matrices.

Comparing the curves shown in Figs. 7a and 8a, for all austenitic grain orientations and throughout the strain range analyzed, it can be observed that the responses of the samples with an austenitic grain embedded in a uniformly oriented matrix loaded in the $[111]_F$ direction are characterized by a higher strength compared to the responses of the samples where the austenitic grain loaded in the corresponding direction is embedded in a multiply oriented ferritic matrix. Similarly, the austenite with a uniformly oriented matrix loaded in the $[100]_F$ direction has a lower strength compared to the corresponding austenite embedded in a multiply oriented ferritic matrix.

In terms of the evolution of the volume fractions of austenite presented in Fig. 8b, the samples with a $[100]_A$-loaded austenitic grain show a nearly complete transformation at the end of the deformation. In contrast, the transformation rates are relatively low for the samples with austenitic grains loaded in the $[110]_A$ and $[111]_A$ directions. Correspondingly, at the end of the loading process, only a small percentage of austenite has transformed into martensite for those orientations. Averaging the final amounts of untransformed austenite for all orientations shown in Fig. 8b leads to an average reduction of austenite of about 40%. This value is assumed to be representative for a polycrystalline sample and is within the experimental range of 25–50% measured for polycrystalline TRIP steel samples at a similar axial strain level [17]. In comparison, the elastic transformation model presented in [28–31], which ignores plastic deformations in the austenitic phase, predicts a near-complete transformation for comparable samples at about 0.1 axial strain. This illustrates the importance of accounting for plastic deformations in the austenite in order to achieve more accurate predictions of the transformation evolution.

5 Concluding remarks

A micromechanical model that can be used to describe the elastoplastic transformation behavior of austenitic grains in multiphase TRIP steels has been developed. The model combines the martensitic phase-transformation model developed by Turteltaub and Suiker [28,30,31] with an FCC single-crystal plasticity model, where the coupling occurs by means of a thermodynamically consistent formulation within a large-deformation framework. The incorporation of crystallographic information allows the thermomechanical responses of single-crystal austenitic samples to be studied in detail. The simulations of elementary loading cases for single-crystal austenitic samples show a strong interaction between phase transformation and plasticity processes. In uniaxial tension and compression, the plastic deformation in the austenite generally delays the transformation process, where the magnitude of the delay depends on the crystallographic orientation of the sample. Nonetheless, for all cases considered, the austenite completely transformed into martensite at axial deformations less than 12 %. In contrast, under simple shear loading, most of the deformation is due to the development of plasticity in the austenite, and only a relatively small amount of austenite transforms into martensite. Under volumetric expansion, the only inelastic mechanism is transformation, whereas under volumetric contraction neither plasticity nor transformation is observed.

In order to study the mechanical response of TRIP steel microstructures, in addition to the model for the austenitic phase, a single-crystal plasticity model for the ferritic phase was implemented. This model includes the effect of nonglide stresses in order to capture the asymmetric yield response of the BCC ferritic phase in the twinning and antitwinning directions. Several TRIP steel microstructural samples were simulated, showing that the mechanical behavior strongly depends on the crystallographic orientations of the individual grains. For a given ferritic matrix, the TRIP steel sample containing a $[111]_A$-loaded austenitic grain shows a higher initial effective strength than samples with an austenite grain loaded in the $[110]_A$ or $[100]_A$ direction. Nonetheless, the strength of the $[100]_A$-loaded sample eventually becomes higher than that of the $[111]_A$-loaded sample due to a faster transformation into a relatively stiff martensitic phase. The simulations indicate that the transformation process is delayed due to the constraining effect of the ferritic matrix and the dissipation from plastic deformations in the austenitic phase.

Acknowledgments The authors highly appreciate discussions on the metallurgical aspects of TRIP steels with Prof. Sybrand van der Zwaag and Dr. Pedro Rivera Diaz del Castillo from the Delft University of Technology, The Netherlands.

References

1. Ball, J.M., James, R.D.: Fine phase mixtures as minimizers of energy. Arch. Ration. Mech. Anal. **100**(1), 13–52 (1987)
2. Bassani, J.L., Ito, K., Vitek, V.: Complex macroscopic plastic flow arising from non-planar dislocation core structures. Mat. Sci. Eng. A **319**(-321), 97–101 (2001)
3. Bhattacharya, K.: Comparison of the geometrically nonlinear and linear theories of martensitic-transformation. Continuum Mech. Therm. **5**(3), 205–242 (1993)
4. Bhattacharyya, A., Weng, G.J.: An energy criterion for the stress-induced martensitic transformation in a ductile system. J. Mech. Phys. Solids **42**, 1699–1724 (1994)
5. Brown, S.B., Kim, K.H., Anand, L.: An internal variable constitutive model for hot working of metals. Int. J. Plast. **5**, 95–130 (1989)
6. Callen, H.B.: Thermodynamics and an Introduction to Thermostatistics. Wiley, London (1985)
7. Clayton, J.D.: Dynamic plasticity and fracture in high density polycrystals: constitutive modeling and numerical simulation. J. Mech. Phys. Solids **53**, 261–301 (2005)
8. Coleman, B.D., Noll, W.: The thermodynamics of elastic materials with heat conduction and viscosity. Arch. Ration. Mech. Anal. **13**(3), 167–178 (1963)
9. Cuiti no, A.M., Ortiz, M.: Computational modelling of single crystals. Model. Simul. Mater. Sci. Eng. **1**, 225–263 (1992)
10. Diani, J.M., Parks, D.M.: Effects of strain state on the kinetics of strain-induced martensite in steels. J. Mech. Phys. Solids **46**(9), 1613–1635 (1998)
11. Fischer, F.D., Reisner, G., Werner, E.A., Tanaka, K., Cailletaud, G., Antretter, T.: A new view on transformation-induced plasticity (TRIP). Int. J. Plast. **16**, 723–748 (2000)
12. Furnémont, Q., Kempf, M., Jacques, P.J., Göken, M., Delannay, F.: On the measurement of the nanohardness of the constitutive phases of TRIP-assisted multiphase steels. Mat. Sci. Eng. A **328**(1–2), 26–32 (2002)
13. Govindjee, S., Mielke, A., Hall, G.J.: The free energy of mixing for *n*-variant martensitic phase transformations using quasi-convex analysis. J. Mech. Phys. Solids **51**, 763 (2003)
14. Hane, K.F., Shield, T.W.: Symmetry and microstructure in martensites. PMA **78**(6), 1215–1252 (1998)

15. Hull, D., Bacon, D.J.: Introduction to Dislocations. 4th edn. Butterworth, Heinmann, London (2001)
16. Idesman, A.V., Levitas, V.I., Stein, E.: Elastoplastic materials with martensitic phase transition and twinning at finite strains: numerical solution with the finite element method. Comput. Methods Appl. Mech. Eng. **173**, 71–98 (1999)
17. Jacques, P.J., Furnémont, Q., Godet, S., Pardoen, T., Conlon, K.T., Delannay, F.: Micromechanical characterisation of TRIP-assisted multiphase steels by in situ neutron diffraction. Philos. Mag. **86**(16), 2371–2392 (2006)
18. Jacques, P.J., Furnémont, Q., Mertens, A., Delannay, F.: On the sources of work hardening in multiphase steels assisted by transformation-induced plasticity. Philos. Mag. A **81**(7), 1789–1812 (2001)
19. Jacques, P.J., Ladrière, J., Delannay., F.: On the influence of interactions between phases on the mechanical stability of retained austenite in transformation-induced plasticity multiphase steels. Metal. Mater. Trans. A **32**, 2759–2768 (2001)
20. Kohn, R.V.: The relaxation of a double-well energy. Continuum Mech. Therm. **3**, 193–236 (1991)
21. Marketz, F., Fischer, F.D.: Micromechanical modelling of stress-assisted martensitic transformation. Model. Simul. Mater. Sci. Eng. **2**, 1017–1046 (1994)
22. Marketz, F., Fischer, F.D.: A mesoscale study on the thermodynamic effect of stress on martensitic transformation. Metal. Mater. Trans. A **26**, 267–278 (1995)
23. Miehe, C., Schröder, J.: A comparative study of stress update algorithms for rate-independent and rate-dependent crystal plasticity. Int. J. Numer. Meth. Eng. **50**, 273–298 (2001)
24. Peirce, D., Asaro, R.J., Needleman, A.: Material rate dependent and localized deformation in crystalline solids. Acta Metall. **31**(12), 1951–1976 (1983)
25. Simo, J.C., Miehe, C.: Associative coupled thermoplasticity at finite strains—formulation, numerical-analysis and implementation. Comput. Methods Appl. Mech. Eng. **98**(1), 41–104 (1992)
26. Stringfellow, R.G., Parks, D.M., Olson, G.B.: A constitutive model for transformation plasticity accompanying strain-induced martensitic transformations in metastable austenitic steels. Acta Metall. Mater. **40**(7), 1703–1716 (1992)
27. Sugimoto, K-I., Mitsuyuki, K., Hashimoto, S.I.: Ductility and strain-induced transformation in a high-strength transformation-induced plasticity-aided dual-phase steel. Metall. Trans. A **23**, 3085–3091 (1992)
28. Suiker, A.S.J., Turteltaub, S.: Computational modelling of plasticity induced by martensitic phase transformations. Int. J. Numer. Meth. Eng. **63**, 1655–1693 (2005)
29. Tjahjanto, D.D., Turteltaub, S., Suiker, A.S.J., van der Zwaag, S.: Modelling of the effects of grain orientation on transformation-induced plasticity in multiphase steels. Model. Simul. Mater. Sci. Eng. **14**, 617–636 (2006)
30. Turteltaub, S., Suiker, A.S.J.: Transformation-induced plasticity in ferrous alloys. J. Mech. Phys. Solids **53**, 1747–1788 (2005)
31. Turteltaub, S., Suiker, A.S.J.: A multi-scale thermomechanical model for cubic to tetragonal martensitic phase transformations. Int. J. Solids Struct. **43**, 4509–4545 (2006)
32. Vitek, V., Mrovec, M., Bassani, J.L.: Influence of non-glide stresses on plastic flow: from atomistic to continuum modeling. Mat. Sci. Eng. A **365**, 31–37 (2004)
33. Wechsler, M.S., Lieberman, D.E., Read, T.A.: On the theory of the formation of martensite. Appl. Phys. A Mater. **197**(11), 1503–1515 (1953)